TRIBHUVAN UNIVERSITY

INSTITUTE OF ENGINEERING

PULCHOWK CAMPUS

DEVELOPMENT AND BENCH-TOP VALIDATION OF ACTIVE ANKLE-FOOT PROSTHESIS

SUBMITTED BY

BIPIN SHRESTHA (PUL077BME012)

SANDIP KUNWAR (PUL077BME034)

SUMIT THAKUR BARAHI (PUL077BME043)

HARI PRASAD GAJUREL (PUL077BME053)

A PROJECT REPORT

SUBMITTED TO

DEPARTMENT OF MECHANICAL AND AEROSPACE ENGINEERING

IN PARTIAL FULFILLMENT OF THE REQUIREMENT FOR THE DEGREE OF

BACHELOR IN MECHANICAL ENGINEERING

DEPARTMENT OF MECHANICAL AND AEROSPACE ENGINEERING

LALITPUR, NEPAL

MARCH 2025

TRIBHUVAN UNIVERSITY

INSTITUTE OF ENGINEERING

PULCHOWK CAMPUS

A PROJECT REPORT ON
DEVELOPMENT AND BENCH-TOP VALIDATION OF ACTIVE ANKLE-FOOT PROSTHESIS

SUBMITTED BY

BIPIN SHRESTHA (PUL077BME012)

SANDIP KUNWAR (PUL077BME034)

SUMIT THAKUR BARAHI (PUL077BME043)

HARI PRASAD GAJUREL (PUL077BME053)

DEPARTMENT OF MECHANICAL AND AEROSPACE ENGINEERING

LALITPUR, NEPAL

MARCH 2025

COPYRIGHT

TRIBHUVAN UNIVERSITY
INSTITUTE OF ENGINEERING, PULCHOWK CAMPUS
DEPARTMENT OF MECHANICAL AND AEROSPACE ENGINEERING

The undersigned certify that they have read, and recommended to the Institute of Engineering for acceptance, a project report entitled **"DEVELOPMENT AND BENCH-TOP VALIDATION OF ACTIVE ANKLE-FOOT PROSTHESIS"** submitted by Bipin Shrestha, Sandip Kunwar, Sumit Thakur Barahi, and Hari Prasad Gajurel in partial fulfillment of the requirement for the degree of Bachelor of Mechanical Engineering.

Supervisor, Dr. Nawaraj Bhattrai
Associate Professor
Department of Mechanical and Aerospace Engineering
IOE, Pulchowk Campus

Supervisor, Biman Rimal
Assistant Professor
Department of Mechanical and Aerospace Engineering
IOE, Pulchowk Campus

External Examiner, Er. Ramraj Khanal
Managing Director
Calcgen Solutions

Committee Chairperson, Dr. Sudip Bhattrai
Assistant Professor
Department of Mechanical and Aerospace Engineering
IOE, Pulchowk Campus

Date: 2025/03/11

ABSTRACT

Traditional prostheses are incapable of fully aiding in human locomotion, resulting in amputees with asymmetric gait patterns, and small stride lengths. Powered prostheses can improve mobility, comfort, and quality of life for amputees of the lower extremities. This project focuses on the design and benchtop validation of a prototype of a powered ankle foot prosthesis. The PAFP utilizes a belt-pulley transmission, driven by an AK-60-6 actuator, and integrates an STM-32 micro-controller to facilitate communication among sensors which includes IMU, encoder, and motor controller in real time. A series of benchtop tests were conducted on the setup to validate the transmission efficiency, control and structural functionality. Experimental validation included backdrivability tests to assess compliance and loading tests to evaluate the motor's torque response to external load. Finally, position tracking was performed to replicate the natural ankle pitch angle profile observed in human gait.

Keywords: *Powered Prosthesis, Human Gait, IMU, STM32, Bench-top Testing, Backdrivibility*

ACKNOWLEDGEMENT

We express our sincere gratitude to the **Department of Mechanical and Aerospace Engineering, IOE, Pulchowk Campus, Lalitpur** for granting us a valuable opportunity to work on a project that enables us to explore, improve, and apply the knowledge and skills we have gained during our Bachelor of Mechanical Engineering studies. We are thankful to our Supervisor, Associate Professor **Dr. Nawaraj Bhattrai** and Assistant Professor **Biman Rimal**, for providing us with valuable feedback during our project. Similarly, we would like to express our gratitude to the **Robotics Club** and **Sabin Shrestha** for valuable assistance during the inception of our project. We also like to thank **CubeMars** for providing the AK60-6 motor for our project.

Bipin Shrestha (PUL077BME012)

Sandip Kunwar (PUL077BME034)

Sumit Thakur Barahi (PUL077BME043)

Hari Prasad Gajurel (PUL077BME053)

.

TABLE OF CONTENTS

LIST OF FIGURES

LIST OF TABLES

ABBREVIATIONS

AFO	Ankle-foot Orthotic
ABS	Acrylonitrile Butadiene Styrene
ADC	Analog Digital Converter
CAN	Controller Area Network
EDA	Electronics Design Automation
EKF	Extended Kalman Filter
ESAR	Energy Storage and Return
EMA	Electromechanical Actuation
FF	Flat foot
FSM	Finite State Machine
HS	Heel Strike
I2C	Inter-Integrated Circuit
IMU	Inertial Measurement Unit
MDF	Maximum Dorsiflexion
PAFP	Powered Ankle-Foot Prosthesis
PLA	Polylactic Acid
PID	Proportional, Integral and Derivative
ROM	Range of Motion
RTOS	Realtime Operating System
SPC-PGT	Stepped-Planet Compound Planetary Gear Transmission
SACH	Solid Ankle-Cushioned Heel
STM	ST Microelectronics
UART	Universal Asynchronous Receiver/Transmitter
UKF	Unscented Kalman Filter
UHMWPE	Ultra-high molecular weight polyethylene

CHAPTER 1: INTRODUCTION

1.1 Background

Lower limb amputation is the most common type of amputation, primarily caused by trauma, infections, diabetes, and untreated chronic diseases. Currently, most users of prosthetic devices are equipped with passive prosthetic legs. Globally, the number of amputees is on the rise. A study done in all 204 countries shows that the number of traumatic amputations alone increased from 370.25 million in 1990 to 552.45 million in 2019 [1]. Despite market availability and low cost, studies show that around (46-95)% of amputees do not make use of these passive devices [2]. This low usage rate of passive prostheses can be attributed to its inability to fully compensate for the functionality and symmetry provided by a natural human leg during walking.

Traditionally prescribed ankle-foot prosthesis cannot produce the same amount of mechanical power as human ankles as they completely rely on passive mechanical components. Plantar flexing muscles in the ankle are responsible for almost 85% of the power generated during walking. On absence of this power, the amputees develop compensating adaptation including increased hip extension [3], overloading on the intact limb, and reduced stance phase.

Passive prosthesis users also have less reliable gaits, shorter step lengths, and are more prone to falling. Another limitation is the increase in hip power and metabolic cost of walking. Trans-tibial amputees expend around 20% more energy in normative walking. Additionally, a passive prosthesis provides no intentional control to the user. Achieving a compliant, symmetric, energy-efficient gait using a prosthesis is a very tough task.

The development of powered trans-femoral prostheses dates back to the 1970s and 1980s, during which an electro-hydraulic knee-torque controller was created and operated using external electronics [4]. Over the past decade, significant advancements have been made in enhancing the adaptability of prosthetic devices for natural walking. Micro-controller

based semi-active prostheses have been introduced, including the Rheo knee (OSSUR) and BiOM's micro-controller-powered ankle-foot. These devices adjust their output behavior to accommodate various locomotion tasks, such as extending the dorsiflexion phase. Hence, powered prosthetic legs have been shown to improve joint kinematic symmetry, enhance load distribution, and reduce lower back muscle activity.

Advancements in control theory and biomedical engineering have extended our capabilities to develop artificial limbs that can mimic natural movement. Powered prostheses are equipped with a system to overcome most of the limitations in conventional prostheses. Users of powered prosthesis experience reduced metabolic energy expenditure and can achieve personalized gait trajectory through some tuning process based on their personal preferences.

1.2 Problem Statement

Trans-tibial amputees encounter difficulties with basic tasks such as walking. While conventional prostheses offer some assistance, their inability to inject energy during walking renders them passive and less effective. The development of motor-controlled actuators and control algorithms can transform these devices into battery-powered active prostheses. Such devices would grant users volitional control, aiding them in performing daily tasks more easily. The development of active prostheses has the potential to address some of the shortcomings of passive ones, decreasing the duration of rehabilitation, and reducing the psychological fear of falling. The major challenge is the control implementation on the leg to gain compliance in the ground contact phase. Thus, development of powered prostheses reduces the physical and psychological barrier, leading to better daily living experiences.

1.3 Objectives

1.3.1 Main Objective

Design and control a powered ankle-foot prosthesis to compare with the normative gait cycle.

1.3.2 Specific Objectives

- To design and fabricate ankle-foot prosthesis.
- To conduct a backdrivability test to evaluate the system's compliance.
- To perform loading test to assess actuator's torque-producing capability.
- To implement PID controller to track the position of the foot.

1.4 System Requirements (For Development/Implementation)

1.4.1 Hardware Used

The major hardware that is used for the project is listed below:

1. STM-32 micro-controller
2. CubeMars Motor: AK-60-6 V1.1, KV140
3. Motor Driver
4. IMU(BNO055)
5. Power Management Circuit
6. Switch
7. Rotary Encoder
8. Li-Po Battery

1.4.2 Software Requirements

The major software and programming languages used in the project are as follows:

1. SOLIDWORKS
2. ANSYS
3. Python
4. C/C++
5. MATLAB

CHAPTER 2: LITERATURE REVIEW

According to [5] the development of knee-ankle-toe active transfemoral prosthetics has been advanced due to the use of both mechanical and neuromuscular models. Mechanical models using the Euler-Lagrange method, which was employed by *Ferris et al.(2005) and Winter (2009)*, have become more popular by providing a precise control of joint movement. Neuromuscular models replicate natural muscle dynamics and reflexes. The control strategies like impedance control, which is done by the Vanderbilt University researchers, and Finite State Machine (FSM), which divides the gait cycle into distinct phases, have further enhanced prosthesis functionality. This paper includes the recent innovation of Lie groups and Lie algebras for more efficient kinematic modeling, and switching control strategies which ensure smoother and more natural gait transitions. These advancements aim to improve the robustness and adaptability of prosthetic systems. We have found that due to the use of Neuromuscular models, this system is less effective due to extensive muscle deficits in amputees.

In paper [6], lower limb amputation above the knee is a significant challenge in mobility. To remove compensation, high-efficiency actuators to copy the natural movement of the human ankle by using features like impedance control during the stance phase and trajectory tracking during the swing phase to enhance user-controlled adaptability. Studies have highlighted the potential benefits of powered prostheses in normalizing gait patterns. For instance, *Heer and Grabowski (2012)* demonstrated that bionic ankle-foot prosthetics could significantly improve walking gait, closely approximating non-amputees. Through this paper, we have found that several challenges remain in adoption and optimization. Key issues include weight, battery, and the need for extensive calibration and tuning for individual users.

2.1 Prostheses

The evolution of prosthetic legs has improved the quality of life for individuals who have lost their limbs due to injury, disease, or congenital conditions. Passive, semi-passive,

and active prostheses have been developed to mimic the normative gait patterns. Passive prostheses are the best choice for individuals with low-level activity. SACH foot simulates plantar flexion at heel strike by the compression of the cushioned heel and provides dorsiflexion by the flexible belting [7]. ESAR foot consists of a heel spring which stores energy during the heel strike and slowly releases the energy as the foot moves forward. The semi-passive ankle-foot prostheses can be used for activities like sit-to-stand or stair ascent/descent. However, the major limitation of the quasi-passive prosthesis is that it cannot inject power into the gait cycle, as biological limbs do [8].

A fully powered prosthesis injects energy into the user's gait, providing a wide range of speed, torque, and power required for various ambulation activities [9]. A powered ankle-foot prosthesis designed and built by Dr Phillip Voglewede and his students at Marquette University uses a four-bar mechanism in combination with a torsional spring to achieve the non-linear stiffness behavior of a human ankle. PoweredFoot one by iWALK developed in MIT Media Lab with both passive and active components to generate human-like power at the ankle joint [7]. The UMass Ankle uses a polycentric design to improve the users' comfort. The lightweight p^2 ankle-foot prostheses use optimized polycentric kinematics design to improve energy efficiency without using springs or clutches while achieving wide ROM and compact dimension [9].

2.2 Gait Analysis

Gait refers to the periodic movement of the limbs, which includes the movements of arms, hips, and legs. Every individual's gait is unique depending on the gait parameters such as step length, stride length, muscle force, velocity, etc [10].

A complete gait cycle is an interval between successive heel strikes of the same leg. The normal gait cycle consists mainly of the stance (contact with ground) and swing phases (no contact with ground). Approximately 60% of the cycle corresponds to the stance phase and 40% to the swing phase. The gait phases can be further subdivided into initial contact or heel strike, flat foot, toe-off, pre-swing, initial swing, mid-swing, and terminal swing [11].

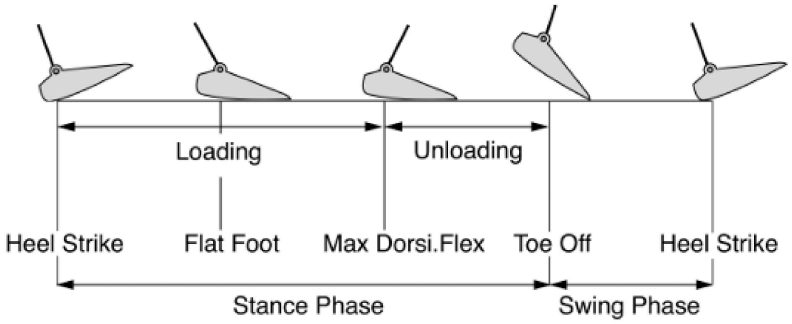

Figure 2.1: Biomechanics of level ground walking [3]

The analysis and characterization of gait parameters is called gait analysis. Through gait analysis, different gait parameters can be available based on which different algorithms can be implemented to determine the gait phases. The selection of appropriate gait parameters determines the extent of estimating the gait phases. Wearable and non-wearable methods are used to monitor and analyze gait parameters [11].

2.2.1 Wearable Method

This method uses sensors such as IMUs, load cells, magnetometers, barometers, force and pressure sensors, Electromyography(EMG), and so on to collect kinematic and kinetic variables.

2.2.2 Non-Wearable Method

This method uses an imaging or motion capture system to record the individual gait cycle. The video is processed and analyzed to obtain the kinematic and kinetic variables such as gait speed, stride length, step size, etc.

2.2.3 Ankle Biomechanics

For the calculation of various gait parameters such as joint angles, powers, and torques, Reznick et al. collected kinematic and kinetic data from ten able-bodied individuals. Markers were placed at specific anatomical locations following the Vicon Plug-in Gait lower body model. The 3-D positions of these markers were captured using ten cameras. A con-

ventional gait model was employed to compute kinematics from the marker data, while inverse dynamics derives the joint kinetics from the force plate data. The dataset provided in [12] can be utilized to develop models for ankle-foot prostheses. The marker placement on the lower limb is based on the Newington-Helen Hayes model on which Plug-in Gait is based.

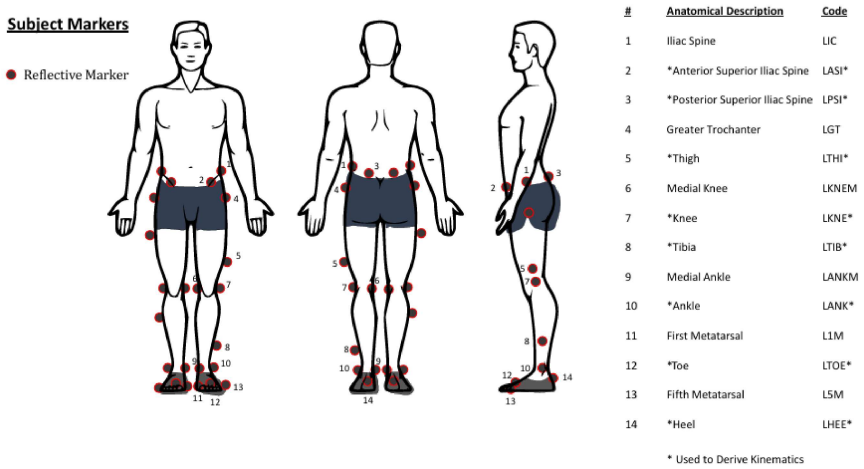

Figure 2.2: Markers placed on left and right limbs symmetrically [12]

An ankle performs significant work during gait, providing positive work during the push-off phase and bearing load during the flat foot stage. The stance phase can be subdivided into controlled plantarflexion (HS to FF), controlled dorsiflexion (FF to MDF), and powered plantarflexion (MDF to TO). Powered plantarflexion contributes over 80% of the mechanical power needed for push-off, propelling the body forward. Three plots visualizing the angle, moments, and power of the ankle for a single stride are shown below:

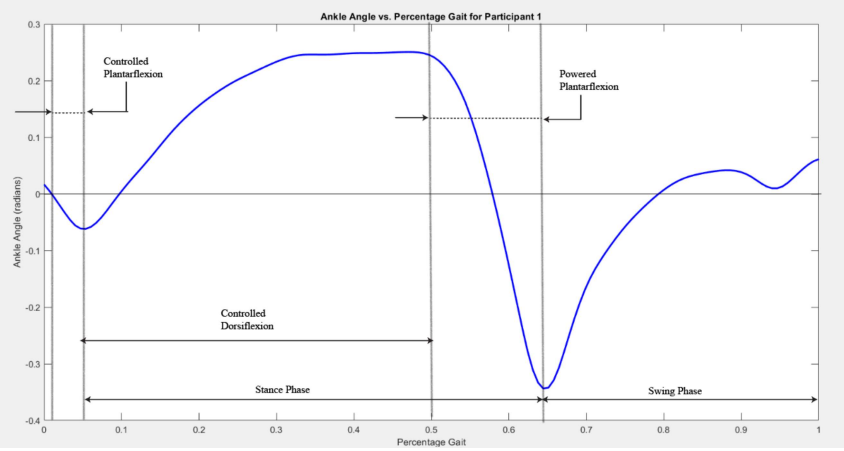

Figure 2.3: Ankle-Angle(rad) v/s % Gait Cycle

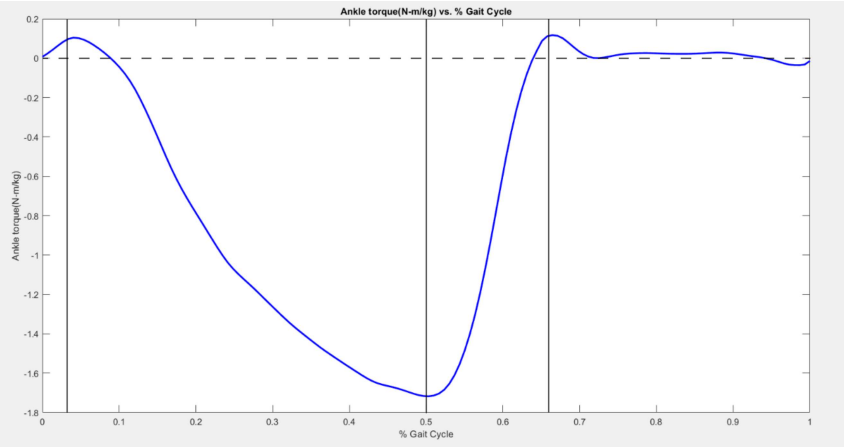

Figure 2.4: Torque(Nm/kg) v/s % Gait cycle

Ankle joint generates significant positive power at the end of the stance phase. The spike observed in the plot at the end of the support phase corresponds to the push-off action. The plantar flexors of the ankle joint generate this power in a normal limb, propelling the body's center of mass (COM) upward and forward. In comparison to other joints, such as the knee and hip, the ankle joint contributes nearly 50 % of the work during walking. In many populations, aging, muscle sclerosis, and the use of old, rigid prosthetics by amputees contribute to a decrease in the propulsive force generated by the ankle. Understanding the role of the ankle in walking allows us to improve the design and power-generation capabilities of the ankle-foot prosthesis.

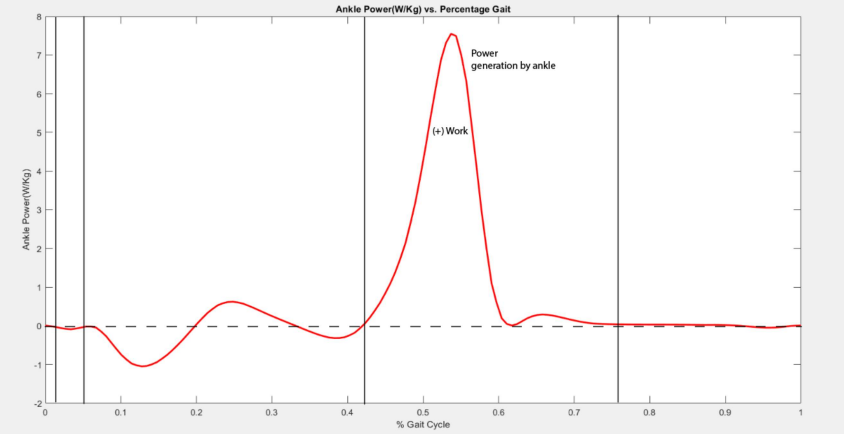

Figure 2.5: Power(W/kg) v/s % Gait Cycle

2.3 Material Selection

Elery et al. used Aluminum 7075-T6 to make the most of the components of the knee-ankle prostheses and stainless steel to make shafts, gears, and bearings[13]. *Kenji* concluded that PLA carbon fiber, manufactured by 3D printing, is the best candidate for the implementation, which can be the material recommendation for the pylon of a leg prosthetic.[14]. *Sarma* designed a CAD model of the ankle-foot orthotic device of different materials such as ABS, PLA, Nylon 6/6, polypropylene, and Kevlar finer reinforced UHMWPE. The model was analyzed in ANSYS Workbench 16.0 software to select the best material for AFO and found that Kevlar Fiber is the best material with a safety factor greater than 1 [15].

2.4 Actuator

In most powered prostheses, movement of joints at the knee and ankle is achieved using an actuator. [16] listed actuators prevalent in the development of prostheses for different ambulation modes. The most common was stiff actuation technology consisting of transmission gear or a belt drive where the actuator is directly coupled to the joint. Series elastic actuators (SEA) were also found to be used because of their compliance and precise force control [17]. Incorporating springs and dampers in series with motors could provide energy

absorption and recovery during motion. This would also increase controller complexity and model uncertainty in model-based control [18]. In addition, the bandwidth of the actuator decreases, causing it to be less responsive to external inputs as it cannot translate the control inputs in a timely and accurate manner.

Modern-day actuators used in robots enable highly dynamic motions. These actuators need to be highly back-drivable, possess high torque density, and be energy efficient [19]. Direct drive, where the motor is directly connected to the load, is technically infeasible because it requires high-torque motors that are impractical in size, weight, and cost. On the other end of the spectrum, using motors coupled with high-ratio gearboxes (as 300:1) introduces issues such as friction, backlash, difficulty in torque prediction, and energy losses.

Elery et al. implemented a quasi-direct drive actuation, which combines the advantages of both direct drive and high gear ratio transmission. This system featured a frame-less, brush-less DC motor integrated into a custom-designed housing, equipped with a 22:1 step planetary gear set. This transmission style offers various reduction ratios without compromising efficiency [8]. The single-stage planetary transmission uses the sun gear as the input and the planet carrier as the output to achieve the maximum reduction ratio.

2.5 Structural Design

Different kinematic designs have been proposed to transmit input torque from the motor to the joint. The 4-bar mechanism is the most used, and polycentric design is advanced prostheses technology. *Cempini et al.* designed a polycentric mechanism characterized by multiple axes of rotation. The p^2 ankle uses a polycentric design, making it lightweight and energy efficient [9].

Elery et al. designed a powered knee-ankle prosthesis with high torque, low-impedance actuators. The brushless DC motor and stepped-planet compound planetary gear transmission (SPC-PGT) were designed in a single house to reduce weight. The input torque was transferred to the ankle using a 4-bar mechanism.

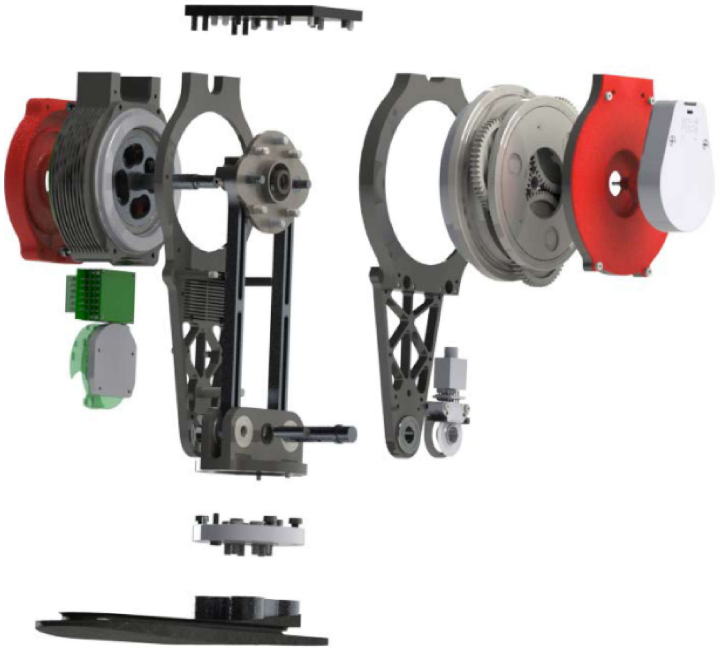

Figure 2.6: 4-bar linkage of Prosthesis[8]

2.6 Control

2.6.1 PID Control

PID is a simple and the most widely used controller for linear systems. It has three terms, corresponding to the error, its integration over time, and its time derivative. The weights for each of these terms are used to control their impacts on the overall control output. The overall control output function of the PID controller in continuous form is

$$u(t) = K_p e(t) + K_i \int_0^t e(\tau \mathrm{d}\tau + K_d \frac{\mathrm{d}e(t)}{\mathrm{d}t} \tag{2.1}$$

In practice, a discrete formulation is used more often, which approximates the integral using quadrature and the derivative using finite difference. The selection of the three coefficients is done through a process called PID tuning. There is a range of techniques for tuning PID controllers; from manual tuning to simple rules on observed system response, to automatic in-loop algorithms that select the best parameters using genetic optimization

or fuzzy search [20].

2.6.2 Finite State Machines

FSM was used to model lower-limb prosthesis controllers using [13]. These states are abstract representations used to manage the behavior of the system. The gait cycle can be divided into discrete phases (heel strike, foot flat, toe-off) referred to as states. This method is popular in prosthesis control as it is simple and flexible in its application. The transition rule between the states is the most important part where the switching rules must be well-defined and measurable [4]. Threshold parameters are typically ground reaction force and joint angles.

Sup et al. created a finite state model shown in Figure 2.7. This same model was also used for walking control in the [8]. The gait phase is subdivided into two sub-phases, stance flexion/extension, pre-swing, swing flexion, and swing extension. The transition parameters are axial load and ankle and knee angle. The threshold value for each parameter is obtained from kinematic data analysis [4]. In state 1, when the ankle angle q_{ankle} reaches the threshold q^{thr}, state 2 begins. Once the foot lifts off the ground, determined when the ground reaction force F_g is less than a threshold F_g^{thr}, the controller switches to state 3. This state ends when the knee velocity, $q_{knee}^{\cdot}$ becomes negative. Finally, the controller starts back at state 1 when the foot strikes the ground in state 4, causing $F_g$to exceed its threshold [18].

Implementing multiple locomotive modes often necessitates additional state and transition rules, which in turn increases the tuning parameters. Therefore, for simple tasks such as walking, a Finite State Machine (FSM) is considered a suitable control technique.

2.6.3 Impedance Control

Impedance control involves regulating the dynamic relationship between force and motion. By adjusting parameters like stiffness, damping, and inertia, robots can interact with their environment in a controlled manner, similar to how human muscles adjust tension during

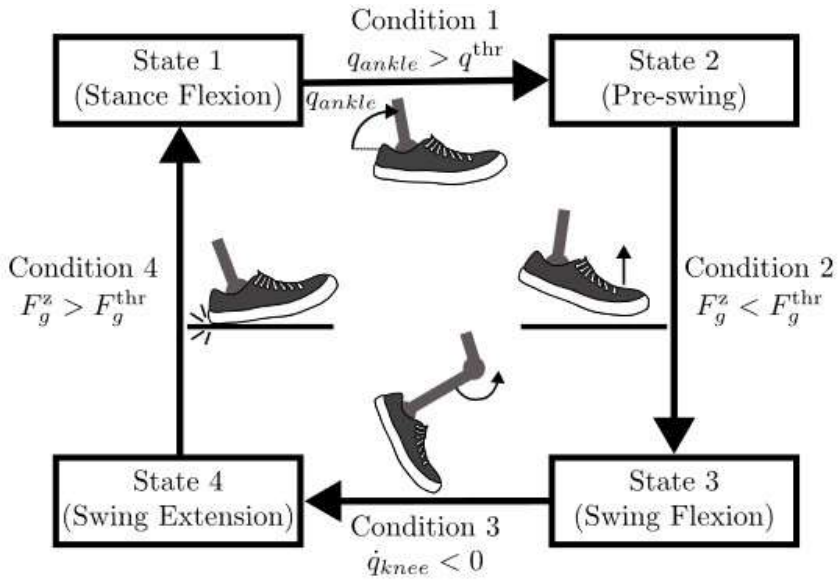

Figure 2.7: Finite State Machine [18]

various activities. Human joints have been shown to behave like a variable impedance controller [18]. Walking is discretized into specific phases (states). For each state, specific impedance control parameters (stiffness, damping, inertia) are defined and held constant while in that state.

The actuator design is particularly effective for compliant walking control paradigms. This is especially crucial when considering the most challenging aspect of mimicking human joint trajectories through position control—the rapid flexion and extension of the knee immediately after impact motivates us to evaluate the actuator's capability to achieve specified impedance behaviors.

Here, joint impedance control is utilized with a joint torque feedback mechanism to achieve the desired behavior. The established relationship between them for a fixed transmission ratio **n** is [6],

$$\tau_j = \tau_m + n^2 I_m \ddot{\theta} + n^2 b_m \dot{\theta} + f(\theta, \dot{\theta}, t) \tag{2.2}$$

where,

τ_m = Commanded torque of the motor.

τ_j = Joint torque of system.

I_m = Inertia of motor

b_m = Damping of motor

θ = Angle at a joint.

The function **f** encompasses nonlinear and time-dependent losses, including effects such as Coulomb friction, stiction, and hysteresis. Also, the torque of the motor is given by

$$\tau_m = nk_t i_m \tag{2.3}$$

where,

k_t = Torque constant of motor.

i_m = Current of motor which is commanded to the driver. The torque feedback is used to decrease the effect of unmodeled dynamics($\boldsymbol{f}$) and I_m and b_m too, but designing an actuator with minimal unmodeled dynamics effectively integrates impedance into the natural dynamics of the system. This approach offers a significant advantage by eliminating the need for a torque sensor. Also, the high noise and limited speed of closed-loop force control provide appropriate passive/natural dynamics. At specified impedance for the actuator to work, they simply set the position control PD gains, K_p and K_d which is equal to the desired spring and damper coefficient. The assumption was made as a fixed angle (Zero) for set position control and moving the ankle joint by hand, which calculates the commanded torque as

$$\tau_m = -K_p\theta - K_d\dot{\theta}.(spring - damperSystem) \tag{2.4}$$

Also, the load cell is used at the joint to measure the applied torque to compare with the commanded torque. Ideally,

$$i.e.\tau_j = \tau_m \tag{2.5}$$

The output proves the effect of un-modeled dynamics is negligible for torque over 10-20 Nm. For low torque ($\boldsymbol{f}$,I_m,b_m) become considerable. A small torque to the end-effector

reveals a noticeable difference between the two torques for amplitudes less than approximately 5 N-m. The difference is around the value obtained from the bench-top back-drive test, which is approximately 3 N-m[8].

2.7 State Estimation

State estimation is a critical component in the control of powered prosthetic devices, allowing for the accurate determination of the prosthesis' state, including position, velocity, and forces. Various methods have been employed to achieve reliable state estimation, including sensor fusion, Kalman filtering, and machine learning approaches. State estimation techniques have been extensively applied in the development and control of powered prostheses. These techniques enable precise control of joint movements, enhance the stability of the device, and improve user comfort. For instance, accurate state estimation allows for the synchronization of prosthetic joint movements with the user's natural gait, leading to more natural and efficient walking patterns.

In the context of the powered polycentric ankle prosthesis discussed in this paper, state estimation is pivotal for achieving desired performance outcomes. The prosthesis utilizes a combination of sensor data and advanced estimation algorithms to maintain optimal functionality across different walking speeds and conditions [9], [21]–[23].

2.7.1 Sensor Fusion

Sensor fusion techniques combine data from multiple sensors to improve the accuracy and robustness of state estimation. This approach leverages the strengths of different sensors to compensate for individual weaknesses. For instance, integrating data from encoders, accelerometers, and gyroscopes can provide comprehensive insights into the prosthesis state. The integration process typically involves algorithms that weigh sensor data based on their reliability and accuracy. Sensor fusion has emerged as a rapidly advancing field due to the increased availability and diversity of sensors, necessitating efficient data integration for enhanced human perception and decision-making capabilities[24].

2.7.2 Kalman Filter

Kalman filters[25] are widely used in state estimation for prosthetic devices due to their effectiveness in handling noisy measurements and providing optimal estimates. These filters operate by predicting the state of the system and then updating this prediction based on sensor measurements. The Kalman filter's recursive nature makes it suitable for real-time applications in prosthetics, where continuous monitoring and adjustment are required. It is optimal as long as the involved models are linear, and the state follows a Gaussian distribution.

The Kalman Filter has two repeating steps: prediction and estimation. The current state x_k is predicted using the previous state $\hat{x}_{k-1}$ and control inputs u_k.

$$x_k = F_k \hat{x}_{k-1} + B_k u_k + w_k \tag{2.6}$$

F_k is the process model, and B_k is the control-input model. Then, sensor readings z_k are integrated with the prediction to obtain a new estimate of the state $\hat{x}_k$.

$$\hat{x}_k = (I - K_k H_k) x_k + K_k z_k \tag{2.7}$$

K_z is the Kalman gain which trades off between the prediction and sensor readings based on their variances. For non-linear processes, two extensions to KF are used. The Extended Kalman Filter [26] uses differentiation to locally linearize the non-linear models. Unscented KF(UKF)[27] transforms a set of sampled points called sigma points through non-linear models, and then recovers a normal distribution from these points.

2.8 Bench-top Testing

To assess the design and control specification of the prosthesis, *Elery et al.* performed several tests in a controlled laboratory environment.

Backdrivability Test

Backdrivability refers to the ability of an actuator to be driven by the load. It characterizes how easily an external force can move the system when the actuator (motor) is not powered. In human-centered robotics, backdrivability is essential for user safety and the actuator's integrity. A system with good backdrivability feels natural and compliant. A powered prosthesis is required to produce high torque for assistance in movement. This torque can be achieved through the use of a high torque motor or low gear ratio. Both of these means have some disadvantages. The high torque motors are larger and are not suitable for locomotive devices. Similarly, having low gear ratio means high inertia. Hence, to achieve high torque, there is a trade-off between the motor and transmission process. *Elery et. al (2020)* performed backdrivability test and measured the torque using a 6-axis load cell.

Backdrive torque (τ_b) is the calculated metric and is defined as the minimum torque to rotate the output at some acceleration and speed [28]. The inertia of the rotating parts and the motor on the load side, is termed as reflected inertia or backdriving inertia. *Lopez Garcia et al. (2022)* developed scaling laws to model the backdrivability and the influence of various design parameters on the torque. For example, the reflected inertia of the rotor in the motor follows the square law with the transmission ratio, i.e, $J_r = J_m * N_t^2$. where J_r and J_m represent reflected and motor inertia, respectively, and N_t refers to the transmission ratio. This scaling is derived from the fundamental concept of inertia.

Rotational inertia depends on N_t^2 and changing the speed ratio affects the mass distribution. If a motor drives a smaller pulley at a higher speed, the output moves slower but with greater force. This causes inertia to increase in the output. Consequently, each transmission stage scales the reflected inertia by the square of its ratio. *Zhu, et al.* calculated the total reflected inertia of their system as:

$$J_{\text{total}} = J_m * N_t^2 + J_t, \tag{2.8}$$

where,

$$J_t = \sum_{i=1}^{n} J_i * N_i^2 \tag{2.9}$$

The subscript i in J_i refers to any rotating components in the transmission, N_i is the speed ratio of the i_{th} rotating component relative to the output. The backdrive torque is then calculated as the product of this total reflected inertia and the angular acceleration of the load. *Zhu, et al. (2022)* modeled the dynamic torque incorporating both the motor and transmission,

$$\tau_b = \frac{J_{\text{total}} * \dot{\omega}}{\eta} \tag{2.10}$$

where,

τ_b = Backdrive Torque

η = Transmission efficiency

$\dot{\omega}$ = Angular acceleration

Loading Test

The loading test is an essential experimental procedure used to examine the mechanical behavior, durability, and efficiency of a system under realistic working conditions. In this study, it is specifically conducted to assess how well the Electromechanical Actuation (EMA) system replicates the natural motion of the human ankle joint. The main goal of this evaluation is to determine whether the prosthesis can generate the necessary torque and velocity while operating under load conditions that closely resemble those experienced in human gait [29].

Objective

The primary objectives of this test include:

1. Evaluating the torque and velocity response of the prosthetic ankle.

2. Confirming that the system effectively mimics the biomechanics of human gait.

3. Ensuring that the prosthesis meets the necessary power, stability, and efficiency requirements.

4. Verifying that the load trajectory aligns with that of a natural ankle joint.

To create a realistic simulation, the actuator applies a counter-torque through angular displacement θ, replicating plantarflexion under elastic loading and ground reaction forces, similar to the stance phase of walking. The ankle follows a controlled sinusoidal angular displacement pattern, which generates the corresponding output torque, expressed mathematically as:

$$\theta = \theta_0 \sin(\omega t) \tag{2.11}$$

$$T_l = -k_l(\theta + \theta_0) \tag{2.12}$$

CHAPTER 3: METHODOLODY

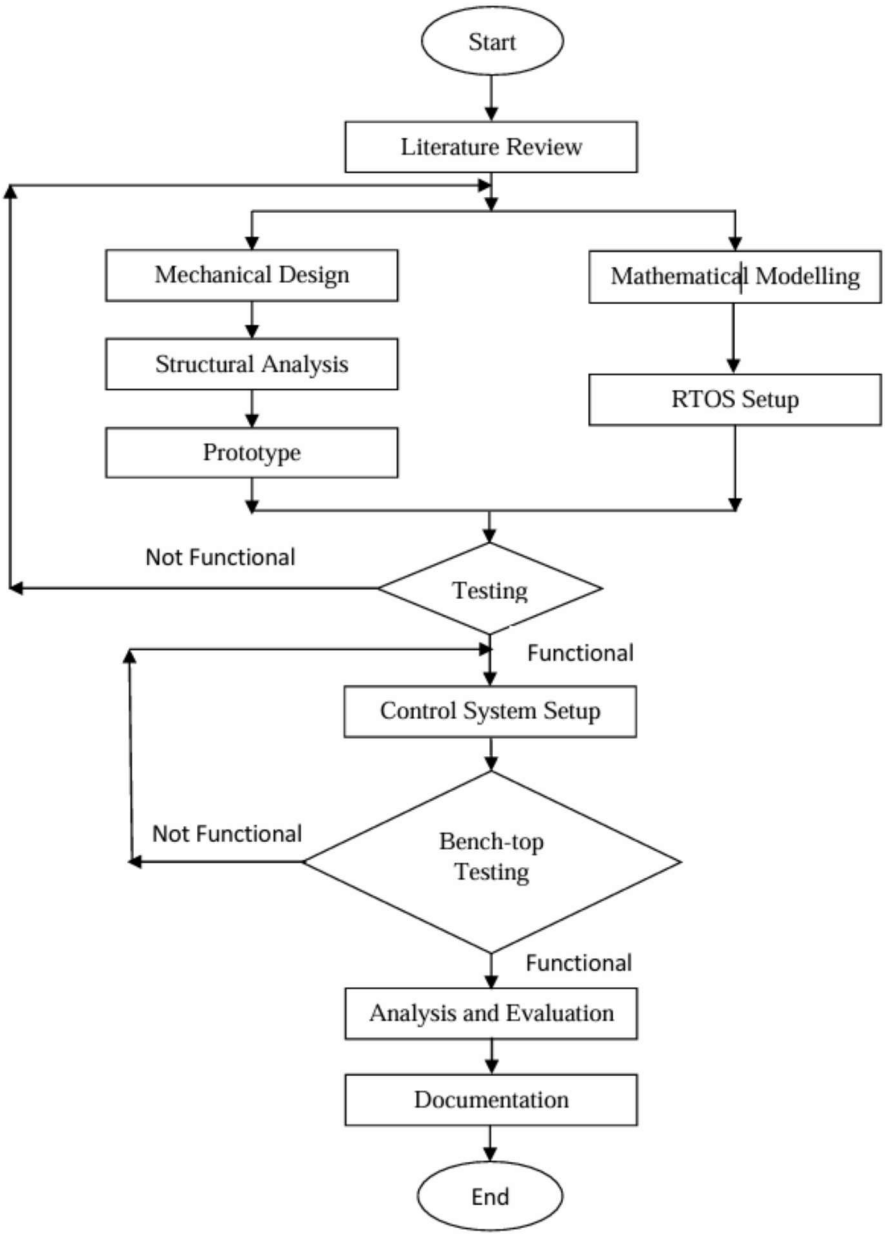

Figure 3.1: Methodology Flowchart

3.1 Prototype Design and Fabrication

A CAD model for an ankle-foot prosthesis was first designed and analyzed in SOLIDWORKS. After completion of modeling the PAFP, each component was 3D printed using PLA plus, except the input pulley, which was machined to enhance its fatigue strength and fracture resistance under multiple cycles. Actuator, encoder, IMU, STM32, and bug converted were integrated to complete the PAFP for the benchtop setup. The detailed design of our prosthesis is presented in Appendix A.

3.2 Transmission Mechanism

The transmission system of our PAFP is designed to transfer torque up to 14 Nm from the actuator to the output pulley. As shown in Figure 3.2, the transmission system consists of a belt-pulley arrangement with a reduction ratio of 4.6, allowing for the required torque to be transmitted to the foot. The input pulley is connected to the output pulley via a polyamide timing belt, which is enclosed in a housing. The output pulley is then linked to the pyramid strut, which transfers the motion to the foot.

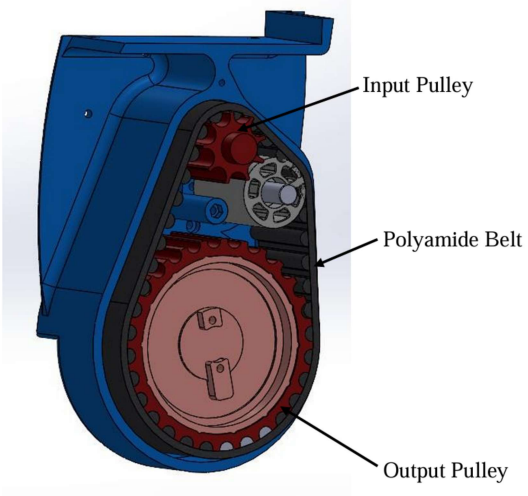

Figure 3.2: Transmission Mechanism

3.2.1 Belt Selection

Output pulley requires 14 Nm torque at 55 rpm. The safety factor is considered to be 1.5 to withstand torque up to 21 Nm at 250 rpm. The HTD 10 mm series belt was chosen based on the Gates PowerGrip GT3 charts having pitch, length, and the number of teeth in the belt are 10 mm, 360 mm, and 36 mm respectively.

The input pulley has a torque rating of 30 Nm, provided by the belt. When adjusted with a length ratio of 0.3 and a width ratio of 1, the torque rating becomes 9 Nm. This results in a factor of safety (FOS) of 2, which is sufficient.

3.2.2 Input Pulley Load Calculation

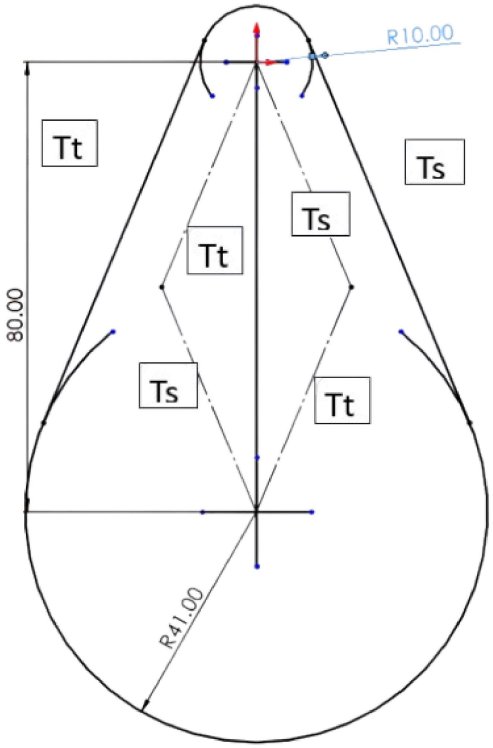

Figure 3.3: Belt pulley vector diagram

T_t = Tight side tension (N)

T_s = loose(slack) side tension (N)

Q = Torque load (Nm)

Pd = Pitch diameter (mm)

1. **Tensions and Resulting Forces**

   Figure 3.4 illustrates the tension distribution in our belt drive system. For a torque of 21 Nm, with a center distance of 80 mm between the pulleys and pitch diameters of approximately 89.127 mm for the output pulley and 19.1 mm for the input pulley, we determine four tension values. Since the belt is used as a registration drive, each tension value is increased by 100 N.

$$\begin{aligned} T_{t,\text{input pulley}} &= 2.5 \times \frac{21}{19.1 \times 10^{-3}} + 100 \text{ N} = 2848.7 \text{ N} \\ T_{s,\text{input pulley}} &= 0.5 \times \frac{21}{19.1 \times 10^{-3}} + 100 \text{ N} = 649.74 \text{ N} \\ T_{t,\text{output pulley}} &= 2.5 \times \frac{21}{89.127 \times 10^{-3}} + 100 \text{ N} = 689 \text{ N} \\ T_{s,\text{output pulley}} &= 0.5 \times \frac{21}{89.127 \times 10^{-3}} + 100 \text{ N} = 217.81 \text{ N} \end{aligned} \tag{3.13}$$

   The vector sum correction factor of 0.92 was calculated using the center-to-center distance and the pitch diameter difference of the pulley using the equation $\frac{D-d}{c} = \frac{89.127-19.1}{80} = 0.875$. The driving force of (2848.7+649.74) × 0.92 = 3218.6 N and a driven force of (689 + 217.81) × 0.92 = 834.27 N is obtained which acts axially at the pulley's shaft. We have set up pulleys on both sides of the pulley's shaft so the radial force on each bearing will be half the total load.

2. **Input Pulley Failure Calculations**

   The input pulley in the system is expected to transmit 3 Nm of torque. The belt and pulley system was designed for this load case following SDP/SI's recommendations. For our specific torque requirement, considered as τ = 4.5 Nm per shaft to ensure a minimum safety factor of 1.5, and a required belt tension of $F_{\text{belt tension}}$ = 100 N, the

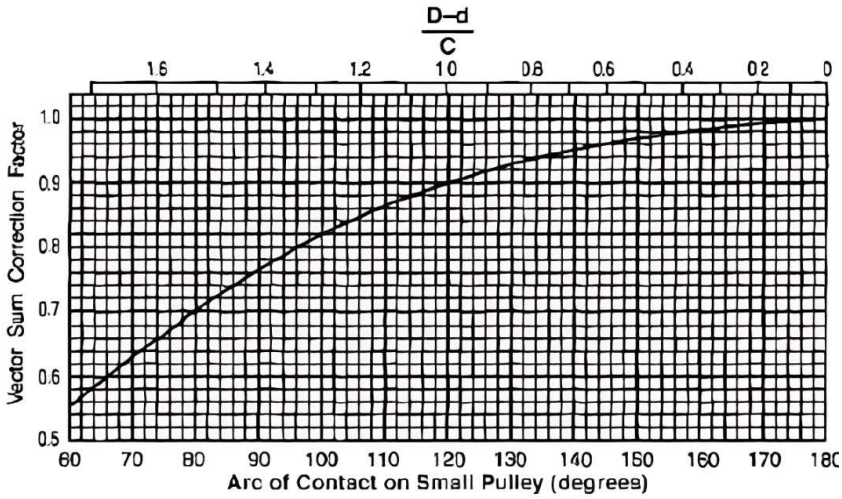

Figure 3.4: Vector Sum Correction Factor

resulting radial force due to the appropriate belt tension and transmitted torque on the input pulley is calculated as $F_{\text{radial equiv}}460.98N$.

Due to the higher effective force of 460.98 N, the input pulley is considered the most critical component. The remaining pulley operates under a lighter load and is therefore deemed safe if designed similarly to the input pulley.

Based on these loads and the system's geometry, the bearing reaction forces and shaft moments were determined. The following calculations outline the key steps in computing the Goodman's line safety factor for the most critical pulley.

$$F_{\text{torque equiv}} = \frac{\tau}{r_{\text{pulley}}} = \frac{4.5 \text{ Nm}}{10 \text{ mm}} = 450 \text{ N} \tag{3.14}$$

$$F_{\text{radial equiv}} = \sqrt{F_{\text{belt tension}}^2 + F_{\text{torque equiv}}^2} = 460.98 \text{ N}. \tag{3.15}$$

Given maximum input pulley bending moment M_{max} of 7.38 Nm (due to the bearing's reaction force) and input pulley's shaft diameter d = 12 mm, the maximum bending stress is

$$\sigma_{max} = \frac{32M_{max}}{\pi d^3} = 43.5 \text{ MPa}, \tag{3.16}$$

With a stress concentration factor K_f = 1.26, the bending stress amplitude is $\sigma_{ba} = K_f \sigma_{max}$ = 54.81 MPa. For a torque of τ = 4.5 Nm, the corresponding shear stress amplitude is,

$$\tau_a = \frac{16\tau}{\pi d^3} = 13.26 \text{ MPa} \tag{3.17}$$

And the Von Mises stress is

$$\sigma'_a = \sqrt{\sigma_{ba}^2 + 3\tau_a^2} = 59.43 \text{ MPa}. \tag{3.18}$$

The ultimate tensile strength S_{ut} of Aluminium Alloy is 310 MPa and the endurance limit S_e is calculated as

$$S_e = \text{Correction Factor} \times 0.5 \times S_{ut} = 0.772 \times 0.5 \times 310 \text{ MPa} = 119.7 \text{ MPa} \tag{3.19}$$

The factor of safety is

$$n_s = \frac{S_e}{\sigma'_a} = 2.01. \tag{3.20}$$

This analysis confirms that even when subjected to twice the expected operating torque, the Goodman's line safety factor remains at 2. This indicates a strong design, demonstrating that the shafts can reliably operate under much higher loads. The shafts are expected to withstand up to approximately 9 Nm—about four times the anticipated operating range before failing. This offers a substantial safety margin, confirming the system's reliability and durability under varying load conditions.

3.3 Structural Analysis

The structural analysis of the input and output pulley was conducted in ANSYS to ensure the ability to withstand the high torque from the actuator. The input pulley is directly connected to the actuator through a coupler, which transmits the motion to the output pulley through a belt, creating 4.6:1 gear reduction. The structural analysis was performed to evaluate the pulley's performance under maximum torque.

3.3.1 Input Pulley

Structural analysis of input pulley was performed to visualize the deformation and stress as it experiences high torque from the actuator. The meshing for the simulation was tetrahedral utilizing a quadratic order. The element size was set to 9.5×10^{-4}m to ensure optimal resolution of the geometry. In the analysis, one end of the pulley, which is directly in contact with the actuator, was subjected to a torque of 4.5 Nm, while the other end was fixed.

Table 3.1: Material Properties

Name	6061 T-6 Aluminium
Yield Strength	270 MPa
Young's Modulus	69 GPa
Tensile Ultimate Strength	310 MPa
Poisson ratio	0.33

3.3.2 Output Pulley

The motion from the input pulley is transmitted to the output pulley through the belt. The output pulley is made from the PLA+ whose material is mentioned in the Table 3.2. The torque applied was 20.7 Nm on the driven portion of the output pulley system. The meshing for the simulation was tetrahedral utilizing a quadratic order. The element size was set to 5 $\times 10^{-4}$m to ensure optimal resolution of the geometry.

Table 3.2: Material Properties of PLA+

Property	**Value**
Name	PLA (Polylactic Acid) plus
Yield Strength	26 MPa
Tensile Ultimate Strength	55 MPa
Young's Modulus	600 MPa
Poisson's Ratio	0.35

3.4 RTOS

A Real-Time Operating System is an operating system in which events are processed in real time, having precise time constraints. It is a very essential component in an embedded system where precise timing and responsiveness are critical. An RTOS provides a task-based approach, allowing multiple tasks to run concurrently while ensuring that each task has access to the necessary resources and executes within a specified time frame.

3.4.1 Hardware Overview

Our system consists of STM32 which communicates with IMU(BNO08x), and rotary encoder. The power circuit drops 12V to 5V to power the encoder and IMU. The encoder connected by the timer provides angular velocity. The motor (CubeMars AK60-6) operates at 24V communicating with the STM32 via UART. Additionally, the IMU, which measures acceleration along three axes and the foot's tip orientation, also interfaces with the STM32 through UART. STM32 communicates in packets while transferring and receiving data. Key data, including pitch(IMU), count(encoder), motor current, and torque, can be observed via laptop terminal. The diagram below illustrates the communication signals along with the hardware used.

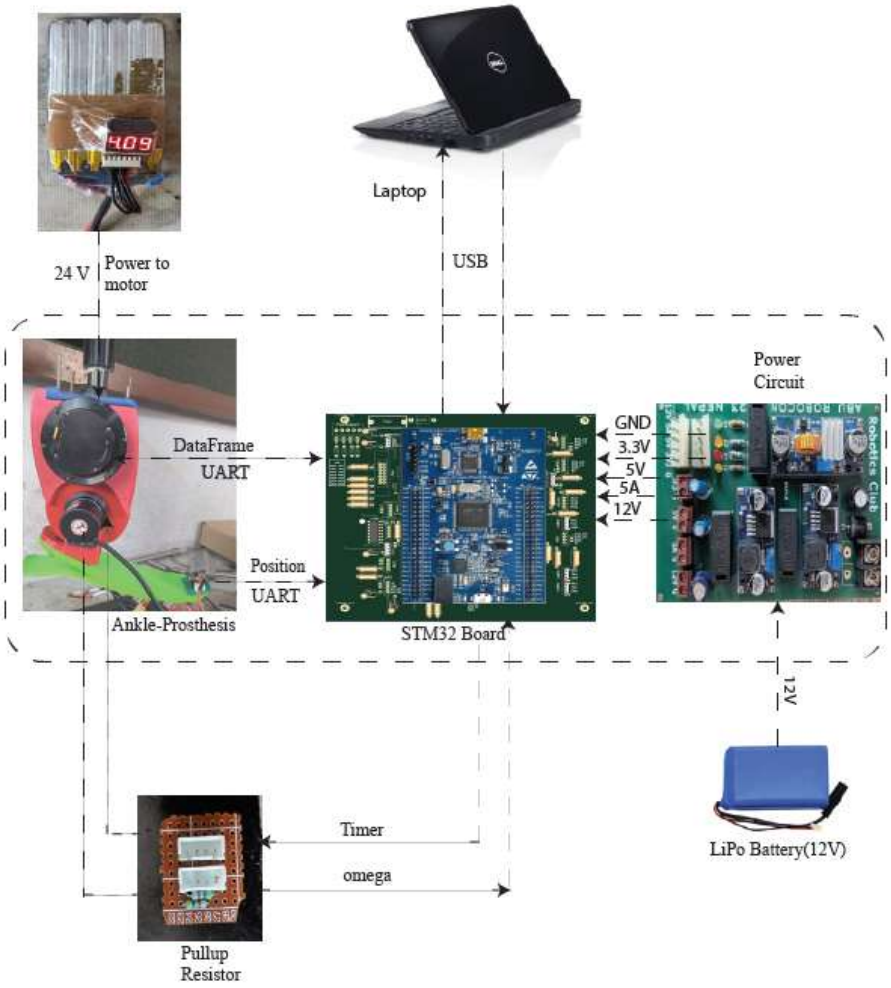

Figure 3.5: Hardware signal flow diagram

3.5 Component Modeling

Component modeling refers to the process of representing physical components in terms of mathematical equations to analyze and design the system. The process involves deriving mathematical models that will describe the action and behavior of individual components.

Modeling the motor, motor driver, IMU, and integrated system helps in understanding the interactions of the parts and developing control strategies.

Modeling of the system is carried out through the system identification process. This process is a data-driven approach where, experiments are conducted to analyze the behavior of the system. In the case of motor, motor driver and IMU, this behaviour is quantified in the form of a transfer function. Additionally, a state-space model is derived to represent the overall response of the system.

We conducted various tests to obtain the model and fit the model. The first-order transfer function is modeled as Equation 3.21, and the second-order transfer function is modeled as Equation 3.22.

$$\frac{Y(s)}{X(s)} = k \cdot \frac{1}{1+\tau s} \tag{3.21}$$

where k is the gain and τ is the time constant.

$$\frac{Y(s)}{X(s)} = k \cdot \frac{\omega^2}{s^2+2\zeta\omega s+\omega^2} \tag{3.22}$$

where k is the gain, ζ is the damping constant, and ω is the undamped natural frequency.

3.5.1 Motor Modeling

The motor's behavior is influenced by assumption :

- The motor's stator is a delta wound type.
- The motor's three phases are symmetric, including their resistance, inductance, and mutual inductance.
- There is no change in rotor reluctance with angle due to a non-salient rotor.

The coupled circuit equation [30] of the stator winding in terms of motor electrical constants is,

$$\begin{bmatrix} V_{as}-V_n \\ V_{bs}-V_n \\ V_{cs}-V_n \end{bmatrix} = \begin{bmatrix} R_s & 0 & 0 \\ 0 & R_s & 0 \\ 0 & 0 & R_s \end{bmatrix} \begin{bmatrix} I_a \\ I_b \\ I_c \end{bmatrix} + p \begin{bmatrix} L_{aa} & L_{ab} & L_{ac} \\ L_{ba} & L_{bb} & L_{bc} \\ L_{ca} & L_{cb} & L_{cc} \end{bmatrix} \begin{bmatrix} I_a \\ I_b \\ I_c \end{bmatrix} + \begin{bmatrix} E_a \\ E_b \\ E_c \end{bmatrix} \tag{3.23}$$

Where R_s is the stator resistance per phase, I_a, I_b, I_c are the stator phase currents, p is the time derivative operator, E_a, E_b, $E_c$are the back EMFs in the respective phases in (1), V_n is the neutral point node voltage given by

$$V_n = \frac{1}{3}\left[V_{as}+V_{bs}+V_{cs}\right] - \sum BEMFs \tag{3.24}$$

The induced EMFs are all assumed to be trapezoidal, whose peak value is given by,

$$E_P = (BLv)N = N(BL\omega) = N\Phi\omega = \lambda\omega \tag{3.25}$$

Where B is the flux density of the field in webers, L is the stator length, N is the number of turns per phase, ω is the electrical angular speed in rad/sec, Φ represents flux linkage $\Phi = BLr$, λ represents the total flux linkage given as the product number of conductors and flux linkage/conductor. If there is no change in the angle of the rotor resistance due to the non-salient rotor and assuming three symmetric phases, inductances and mutual inductances are assumed to be symmetric for all phases as in [30]. Hence the above equation becomes,

$$\begin{bmatrix} V_a \\ V_b \\ V_c \end{bmatrix} = R_s^* \begin{bmatrix} 1 & 0 & 0 \\ 0 & 1 & 0 \\ 0 & 0 & 1 \end{bmatrix} \begin{bmatrix} I_a \\ I_b \\ I_c \end{bmatrix} + p \begin{bmatrix} L & M & M \\ M & L & M \\ M & M & L \end{bmatrix} \begin{bmatrix} I_a \\ I_b \\ I_c \end{bmatrix} + \begin{bmatrix} E_a \\ E_b \\ E_c \end{bmatrix} \tag{3.26}$$

Simplifying (4) further we get the following

$$\begin{bmatrix} V_a \\ V_b \\ V_c \end{bmatrix} = R_s^* \begin{bmatrix} 1 & 0 & 0 \\ 0 & 1 & 0 \\ 0 & 0 & 1 \end{bmatrix} \begin{bmatrix} I_a \\ I_b \\ I_c \end{bmatrix} + p \begin{bmatrix} L-M & 0 & 0 \\ 0 & L-M & 0 \\ 0 & 0 & L-M \end{bmatrix} \begin{bmatrix} I_a \\ I_b \\ I_c \end{bmatrix} + \begin{bmatrix} E_a \\ E_b \\ E_c \end{bmatrix} \tag{3.27}$$

The generated electromagnetic torque is given by

$$T_e = \frac{E_a I_a + E_b I_b + E_c I_c}{\omega} \quad \text{(in Nm)} \tag{3.28}$$

The induced EMFs can be written as,

$$E_a = f_a(\theta)\lambda\omega \tag{3.29}$$

$$E_b = f_b(\theta)\lambda\omega \tag{3.30}$$

$$E_c = f_c(\theta)\lambda\omega \tag{3.31}$$

Where $f_a(\theta), f_b(\theta), f_c(\theta)$ are functions having the same shapes as back EMFs. The values from 2.12 can be substituted in 2.16 to obtain the value of torque. Also,

$$J\frac{d\omega}{dt} + B\omega = T_e - T_l \tag{3.32}$$

where T_l is the load torque, J is the moment of inertia, B is the friction coefficient. Electrical rotor speed and position are related by

$$\frac{d\theta}{dt} = \left(\frac{P}{2}\right) \cdot \omega \tag{3.33}$$

Where P is the number of poles in the motor. From the above equations, the system state

equations are written in the following form.

$$\dot{\mathbf{x}}(t) = A\mathbf{x}(t) + B\mathbf{u}(t) \tag{3.34}$$

Where the states are chosen as

$$x(t) = \begin{bmatrix} I_a \\ I_b \\ I_c \\ \omega \\ \theta \end{bmatrix}^T \tag{3.35}$$

Thus, the system matrices are given below.

$$A = \begin{bmatrix} -R_s/L_1 & 0 & 0 & (\lambda_p * f_\alpha(\theta))/J & 0 \\ 0 & -R_s/L_1 & 0 & (\lambda_p * f_b(\theta))/J & 0 \\ 0 & 0 & -R_s/L_1 & (\lambda_p * f_c(\theta))/J & 0 \\ (\lambda_p * f_\alpha(\theta))/J & (\lambda_p * f_b(\theta))/J & (\lambda_p * f_c(\theta))/J & -B/J & 0 \\ 0 & 0 & 0 & P/2 & 0 \end{bmatrix} \tag{3.36}$$

$$B = \begin{bmatrix} 1/L_1 & 0 & 0 & 0 \\ 0 & 1/L_1 & 0 & 0 \\ 0 & 0 & 1/L_1 & 0 \\ 0 & 0 & 0 & -1/J \\ 0 & 0 & 0 & 0 \end{bmatrix} \tag{3.37}$$

The input vector is defined as

$$u(t) = [V_a, V_b, V_c, T_i]^T \tag{3.38}$$

Where $L_1 = L - M$, L is the self inductance of the winding per phase, M is the mutual inductance per phase and V_a, V_b, V_c are the per phase impressed voltage on the motor windings. Using the above state space model and the parameters, the motor transfer function is

obtained as:

$$\frac{Y(s)}{X(s)} = \frac{23.21 * 10^6}{s^2 + 1476.1955 + 3.261 * 10^9} \tag{3.39}$$

3.5.2 Transfer Function Validation

To validate the transfer function of the motor, we first model it and analyze its step response. The oscillations observed in the response are due to the system's natural frequency. We then validate the model by applying a step response to the actual motor and comparing the results to ensure accuracy

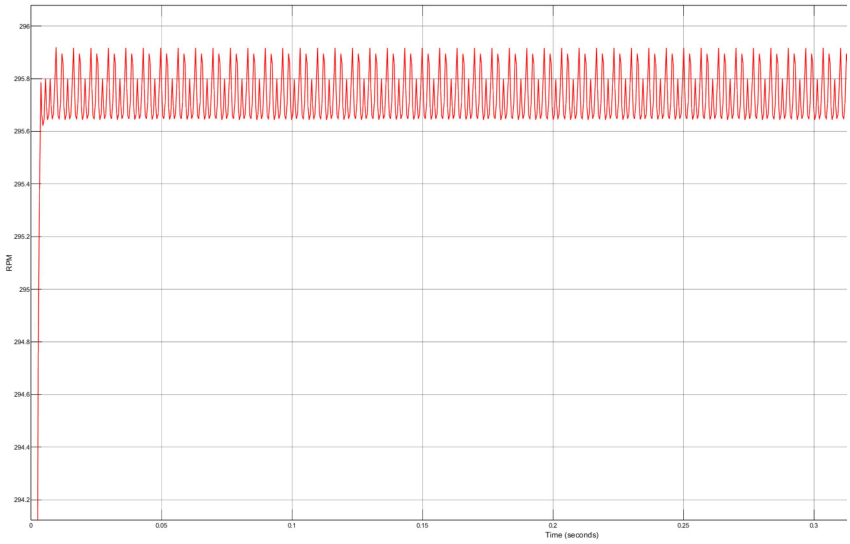

Figure 3.6: Motor Model Response

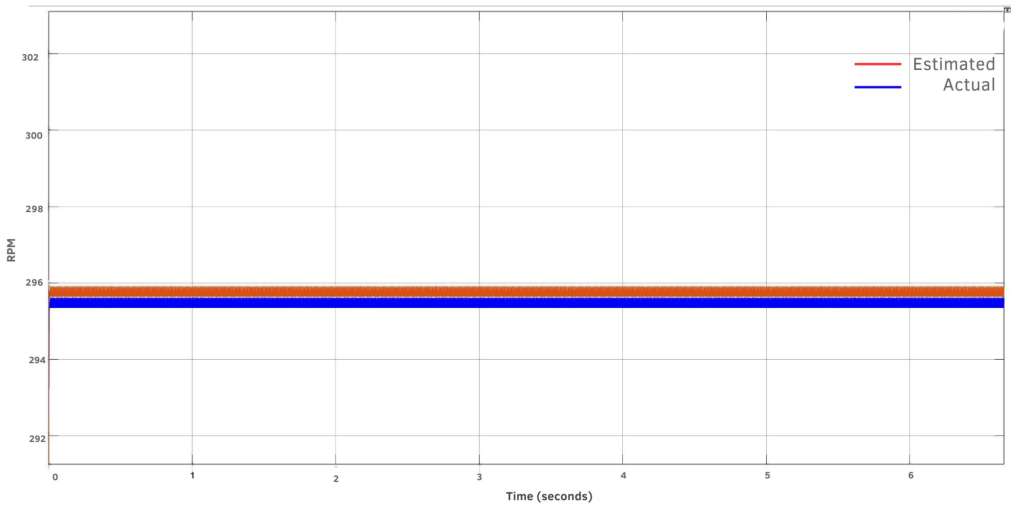

Figure 3.7: Comparison of actual and estimated speed

The graph 3.7 shows that the actual and estimated response of the motor are nearly identical, which indicates parameter estimation is correct. The transfer function we obtain is equivalent to the motor's transfer function.

3.5.3 FOC Driver

Field-Oriented Control (FOC) is a form of vector control used in Permanent Magnet Synchronous Motors (PMSM). In FOC, the stator current, voltage, and magnetic flux are expressed as space vectors in a rotating reference frame (RRF). The main principle is to separate the control of torque and flux, to enable precise motor operation. The phases of a PMSM in the stator can be modeled as RL circuits. The stator voltage $U_{\mathrm{ds}}(s)$ and current $I_{\mathrm{ds}}(s)$ are captured by the first-order transfer function.

$$H_d(s) = \frac{I_{ds}(s)}{U_{ds}(s)} = \frac{1/R_s}{1+sL_d/R_s} = \frac{K_1}{1+sT_1} \tag{3.40}$$

This transfer function represents the dynamic behavior of the stator's circuit, where K_1 is a gain factor, and T_1 is the time constant of the RL circuit.

Time Delay Measurement: The time response of the FOC driver is characterized by an experiment. 24V, constant voltage is supplied to the driver with the motor connected to its output terminal. The system's voltage response is measured by a sensor, and the time delay between input and output voltages is observed. The time constant τ is obtained from this delay.

From this time delay, a first-order transfer function is obtained:

$$\frac{Y(s)}{X(s)} = \frac{24}{1+0.00114s} \tag{3.41}$$

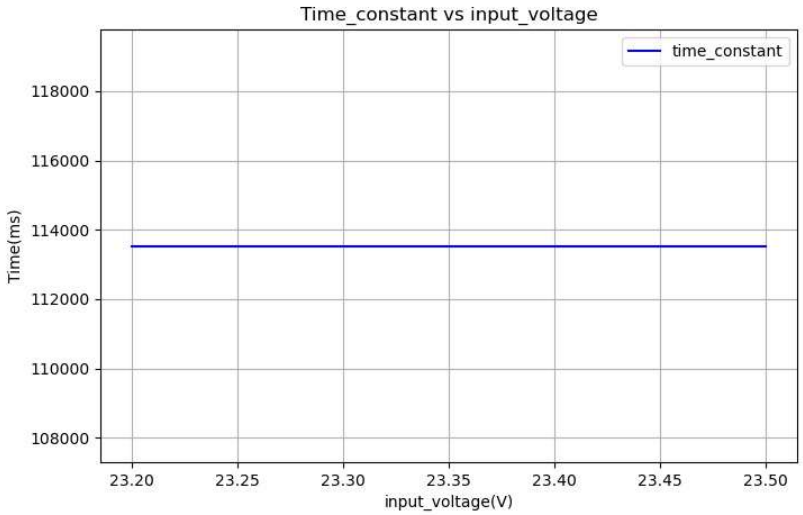

Figure 3.8: Time response of FOC driver: Input Voltage vs Time(ms)

3.5.4 IMU Modeling

The integrated circuit BNO-08x sensor Module is a 9-axis motion device integrating 3-axis Gyroscope, 3-axis Accelerometer, 3-axis magnetometer, and Digital motion processor. It operates at 5V DC and provides real-time motion tracking capabilities.

In system analysis, the step response is used to evaluate the empirical model of a system. The time constant τ of a first-order system corresponds to 63.2% of the rise time. The BNO-

08x measures platform angles in real-time and transmits values from its accelerometer and gyroscope sensors to an STM32 microcontroller via the UART communication protocol. When the sensor is placed in a vertical position on a plane, it provides consistent data. When changes are applied to the system, variations in the angle are observed.

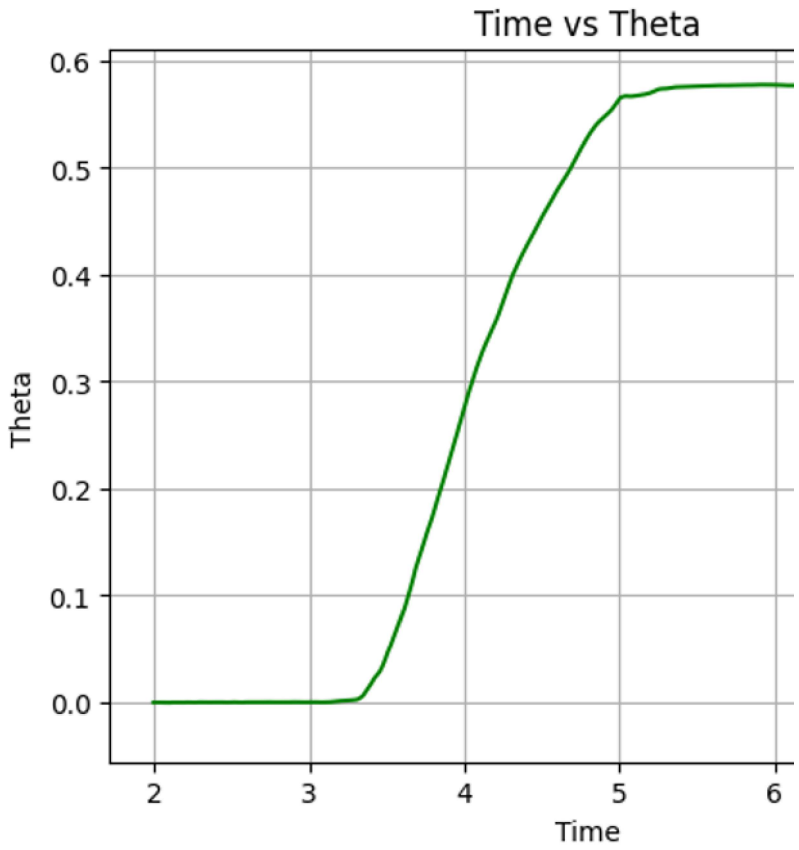

Figure 3.9: Angle vs Time plot of Sensor

The graph 3.9 above shows how the angle changes over time after a quick impulse is applied. Because the sensor has a very fast response time, we can calculate the time delay by using a scatter plot that compares the angle and time from two sets of measured data. This graph displays the scatter plot of these two data sets.

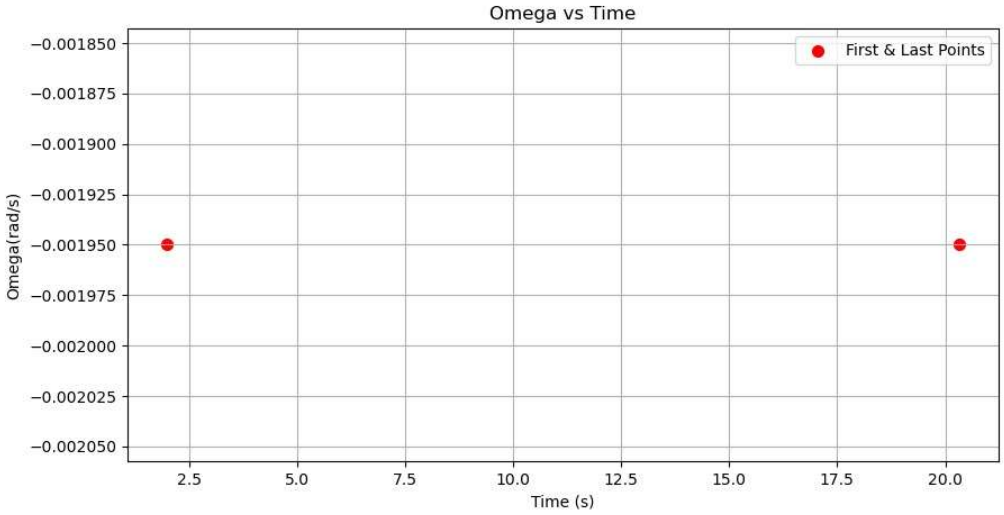

Figure 3.10: Scatter plot of data

From the graph 3.10, we calculate the time difference between two data points, which gave us the time constant 0.0195 seconds. Taking the gain of 1, the first order transfer function is obtained as,

$$\frac{Y(s)}{X(s)} = \frac{1}{1+0.0195s} \tag{3.42}$$

3.5.5 Encoder

We need to measure the feedback angular rate of the outer pulley as input for the Proportional Integral (PI) controller. This is achieved by using a quadrature encoder fitted to the outer pulley. The quadrature encoder has two channels, each producing a set of pulses that are out of phase with each other. By decoding the pulses from both channels, we can determine the angular velocity and direction of rotation.

We utilized a timer on the STM32 microcontroller in encoder mode, which processes the pulses from the encoder and stores the count in the timer's CNT register. When the encoder mode is configured, the count value increases. Our goal is to compute the angular velocity based on this count. The encoder we are using has a resolution of 4000 counts per

revolution (CPR).

Let us suppose we have δ counts in the duration of the sample time is δ t in seconds. We can compute the frequency of motor using the expression

$$f = \frac{\delta c}{\delta t} \frac{1}{CPR} \tag{3.43}$$

Angular velocity of outer pulley can simply be determined as

$$\omega = 2\pi f \tag{3.44}$$

3.5.6 Leg Dynamic Model

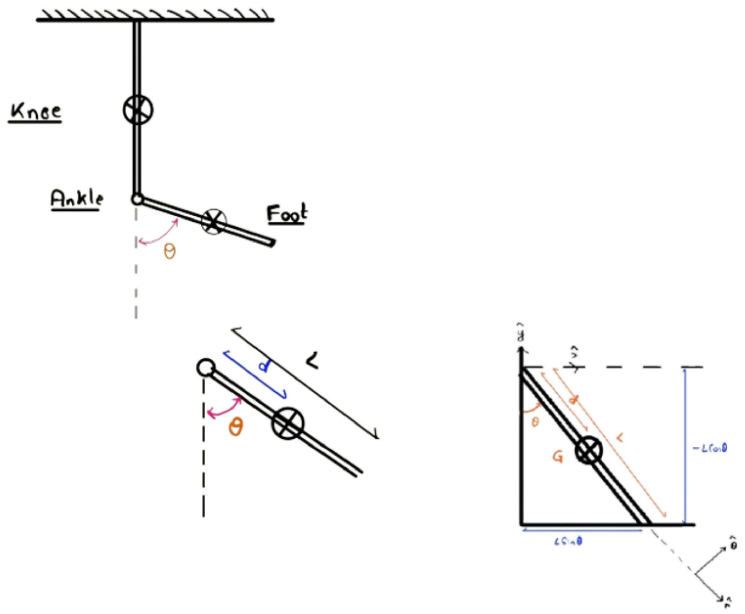

Figure 3.11: Free Body Diagram of the System

The FBD is a simplified representation of the lower limb, focusing on the kinetic chain from ankle to foot. It is used to analyze the forces and torques acting on the system.

Using Euler-Lagrange method, we derived the equation of the torque. The generalized coordinate is the angle θ that describes the rotation of the foot segment around the ankle joint.

The kinetic energy of the system consists of the rotational kinetic energy due to the angular velocity $\dot{\theta}$ and the translational kinetic energy due to the motion of the center of mass.

The rotational kinetic energy is given by:

$$T_{\text{rot}} = \frac{1}{2} J_c \dot{\theta}^2 \tag{3.45}$$

where J_c is the moment of inertia about the center of mass.

The translational kinetic energy is given by:

$$T_{\text{trans}} = \frac{1}{2} m v^2 \tag{3.46}$$

where, $v = d\dot{\theta}$ is the linear velocity of the center of mass, and d is the distance from the ankle joint to the center of mass.

Therefore, the total kinetic energy is:

$$T = \frac{1}{2} J_c \dot{\theta}^2 + \frac{1}{2} m (d\dot{\theta})^2 = \frac{1}{2} (J_c + m d^2) \dot{\theta}^2 \tag{3.47}$$

The potential energy is due to the gravitational force acting on the center of mass. It is given by:

$$V = mgd(1 - \cos\theta) \tag{3.48}$$

where g is the acceleration due to gravity.

The Lagrangian is defined as the difference between the kinetic and potential energies:

$$L = T - V = \frac{1}{2}(J_c + md^2)\dot{\theta}^2 - mgd(1 - \cos\theta) \tag{3.49}$$

The Euler-Lagrange equation for a generalized coordinate θ is:

$$\frac{d}{dt}\left(\frac{\partial L}{\partial \dot{\theta}}\right) - \frac{\partial L}{\partial \theta} = T_d \tag{3.50}$$

where T_d is the external torque applied at the ankle joint.

Compute the partial derivatives:

$$\frac{\partial L}{\partial \dot{\theta}} = (J_c + md^2)\dot{\theta} \tag{3.51}$$

$$\frac{d}{dt}\left(\frac{\partial L}{\partial \dot{\theta}}\right) = (J_c + md^2)\ddot{\theta} \tag{3.52}$$

$$\frac{\partial L}{\partial \theta} = -mgd\sin\theta \tag{3.53}$$

Substitute into the Euler-Lagrange equation:

$$(J_c + md^2)\ddot{\theta} + mgd\sin\theta = T_d \tag{3.54}$$

This is the derived equation of torque using the Euler-Lagrange method. It matches the given equation in the document:

$$(J_c + md^2)\ddot{\theta} + k\dot{\theta} + mgd\sin\theta = T_d \tag{3.55}$$

where an additional damping term $k\dot{\theta}$ has been included to account for energy dissipation

in the system.

$$\begin{aligned} x_1 &= \theta \quad \text{(angular position)} \\ x_2 &= \dot{\theta} \quad \text{(angular velocity)} \\ x_3 &= i \quad \text{(current in motor)} \end{aligned} \tag{3.56}$$

$$(J_c + md^2)\ddot{\theta} + k\dot{\theta} + mgd\sin\theta = T_d \tag{3.57}$$

For this equation, a small change in angle

$$\sin\theta \approx \theta \tag{3.58}$$

Then the above equation becomes:

$$(J_c + md^2)\ddot{\theta} + k\dot{\theta} + mgd\theta = T_d \tag{3.59}$$

Simplify this equation :

$$\ddot{\theta} = \frac{-mgd\theta - k\dot{\theta} + T_d}{J_c + md^2} \tag{3.60}$$

We know that $T_d = K_t i$ Then the above equation becomes:

$$\ddot{\theta} = \frac{-mgd\theta - k\dot{\theta} + K_t i}{J_c + md^2} \tag{3.61}$$

We are using the motor and the electrical equation be :

$$V = L\frac{di}{dt} + Ri + k_e\dot{\theta} \tag{3.62}$$

Again,

$$\frac{di}{dt} = \frac{V - R_i - k_e\dot{\theta}}{L} \tag{3.63}$$

$$\begin{aligned} x_1 &= \theta \\ \dot{x_1} &= x_2 \end{aligned} \tag{3.64}$$

$$\dot{x_2} = \frac{-mgdx_1 - kx_2 + k_t x_3}{J_x + md^2} \tag{3.65}$$

Then v = u (input voltage)

$$\dot{x_3} = \frac{u - Rx_3 - k_e x_2}{L} \tag{3.66}$$

The state space equation is obtained as

$$\begin{bmatrix} \dot{x}_1 \\ \dot{x}_2 \\ \dot{x}_3 \end{bmatrix} = \begin{bmatrix} 0 & 1 & 0 \\ \frac{-mgd}{J_c+md^2} & \frac{-k}{J_c+md^2} & \frac{K_t}{J_c+md^2} \\ 0 & \frac{-K_e}{L} & \frac{-R}{L} \end{bmatrix} \begin{bmatrix} x_1 \\ x_2 \\ x_3 \end{bmatrix} + \begin{bmatrix} 0 \\ 0 \\ 1/L \end{bmatrix} u(t) \tag{3.67}$$

$$\hat{y} = \begin{bmatrix} 1 & 0 & 0 \end{bmatrix} \begin{bmatrix} x_1 \\ x_2 \\ x_3 \end{bmatrix} \tag{3.68}$$

$$\dot{x} = Ax + Bu \tag{3.69}$$

$$\hat{y} = Cx \tag{3.70}$$

where,

$$A = \begin{bmatrix} 0 & 1 & 0 \\ \frac{-mgd}{J_c+md^2} & \frac{-k}{J_c+md^2} & \frac{K_t}{J_c+md^2} \\ 0 & \frac{-K_e}{L} & \frac{-R}{L} \end{bmatrix} \tag{3.71}$$

$$B = \begin{bmatrix} 0 \\ 0 \\ 1/L \end{bmatrix} \tag{3.72}$$

$$c = \begin{bmatrix} 1 & 0 & 0 \end{bmatrix} \tag{3.73}$$

We get the state space model of our system with the dynamics model.

3.6 Control system Design

After modeling each component and placing it within the required controller in a closed-loop system, the control system will correctly read the joint angle and follow the trajectory of the human leg joint angle data. We will then analyze the system's stability and evaluate

how the control system is designed for our application.

3.6.1 Response of uncontrolled system

The unstable behavior of the PAFP was observed with the given initial pi/5 conditions. During bench-top testing, we suspended our system, with the fulcrum located at the bottom of the pulley in our robotic system, causing it to act as an inverted pendulum. The initial position serves as a step input to the system without a controller. As a result, the foot position falls from early stance to late stance within 0.5 seconds, as shown in the figure, further indicating instability.

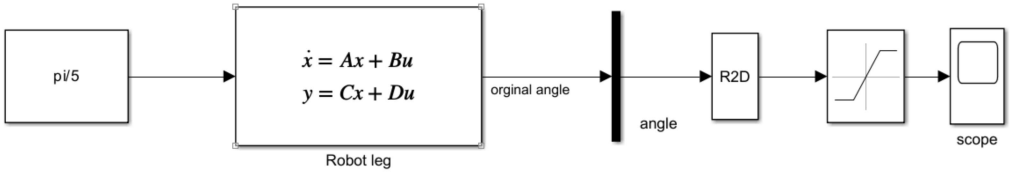

Figure 3.12: Block diagram of the uncontrolled system

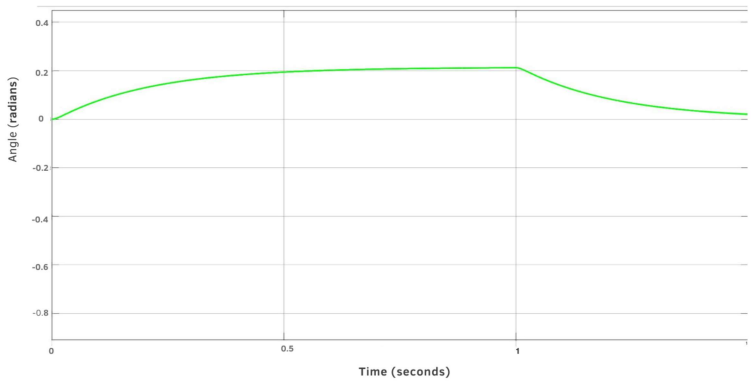

Figure 3.13: Graph of uncontrolled Response

3.6.2 Open loop system

The open loop modeling couldn't make the robot stable. However, open loop modeling is crucial for the sampling time required for PAFP. The impulse is given to the system so that the system may be subject to a sudden change in the gate pulse of the driver which generates the voltage. The graph suggests that the optimal sampling time is 0.9 sec to our system.

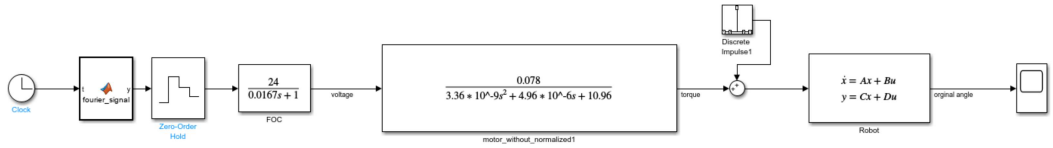

Figure 3.14: Open loop system

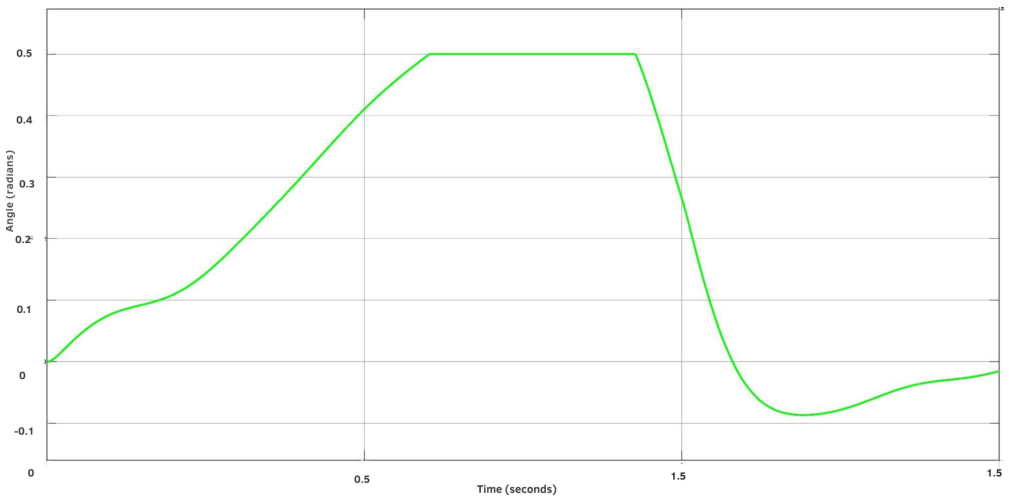

Figure 3.15: Open loop response

3.6.3 Closed Loop System

The robot is unstable and uncontrollable in an open-loop configuration. So, to make it stable, closed-loop control must be designed with a suitable controller. Since disturbance is inherently present in the system, it must be incorporated into the control system to simulate real-world disturbances. In the context of control, a PID controller will be implemented, providing the control signal:

$$U(t) = K_p \cdot e(t) + K_i \int e(t)dt + K_d \frac{d}{dt} e(t) \quad \cdots \tag{3.74}$$

where, $U(t)$ is the controller output, $e(t)$ is the error, K_p, K_i, and K_d are the proportional, integral, and derivative gains, respectively.

In the case of a discrete-time PID controller, the control output is given by:

$$u[k] = K_p \cdot e[k] + K_i \cdot i[k] + K_d \cdot d[k] \quad \cdots \tag{3.75}$$

where,

$$i[k] = i[k-1] + T_s \frac{e[k] + e[k-1]}{2} \tag{3.76}$$

$$d[k] = \frac{e[k] - e[k-1]}{T_s} \tag{3.77}$$

The discrete PID has a saturation limit of ± 1, which is then discretized by order one hold circuits. Thus, we can say that our robot is hybrid with such discrete control.

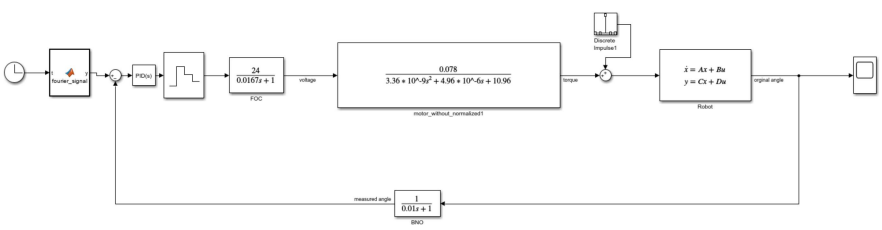

Figure 3.16: Closed loop system

The joint angle data, which varies with time, influences the control system, requiring precise regulation to ensure stability and performance. The PID controller will generate the pulses that are sampled by hold circuits. Correct sampling time is essential for this system as it discretizes the circuit, allowing changes in state only after each sampling interval.

The generated control signal is then fed into the Field-Oriented Control (FOC) driver, which is modeled as a first-order system, suggesting that it will introduce a certain delay in the circuit. The power supply of 24V indicates that the voltage will vary between -24V and +24V, which is then supplied to the motor to drive its operation.

The motor takes input of voltage and gives RPM as voltage is then passed to the block that converts it to the equivalent torque. The torque is fed to the robot model, which gives both position and angle. The angle is then fed to a sensor that provides the correct angle to follow the dynamics of the system.

3.6.4 Position-velocity Loop

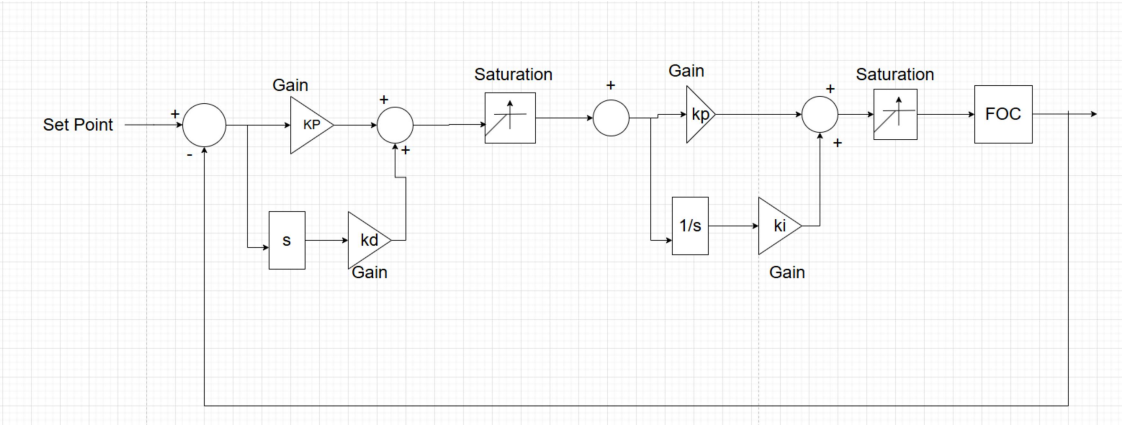

Figure 3.17: Position velocity Loop

The above is the cascaded control loop of the position and velocity of the prosthetic. From the above block diagram to control angular rate, proportional and integral controller is enough because it ensures smooth and stable speed regulation without unnecessary complexity. To control angular position, we must include a derivative controller to control the

position of the system. The controller must have an idea of how fast the system is evolving, the rate of change.

3.6.5 Simulation

The control system designed was simulated using MATLAB/SIMULINK. The simulation provided an overview of the component arrangement and allows for the tuning of PID control gains, enabling the PAFP to follow the desired trajectory within the limits of the components used. The PAFP operates in a controlled environment.

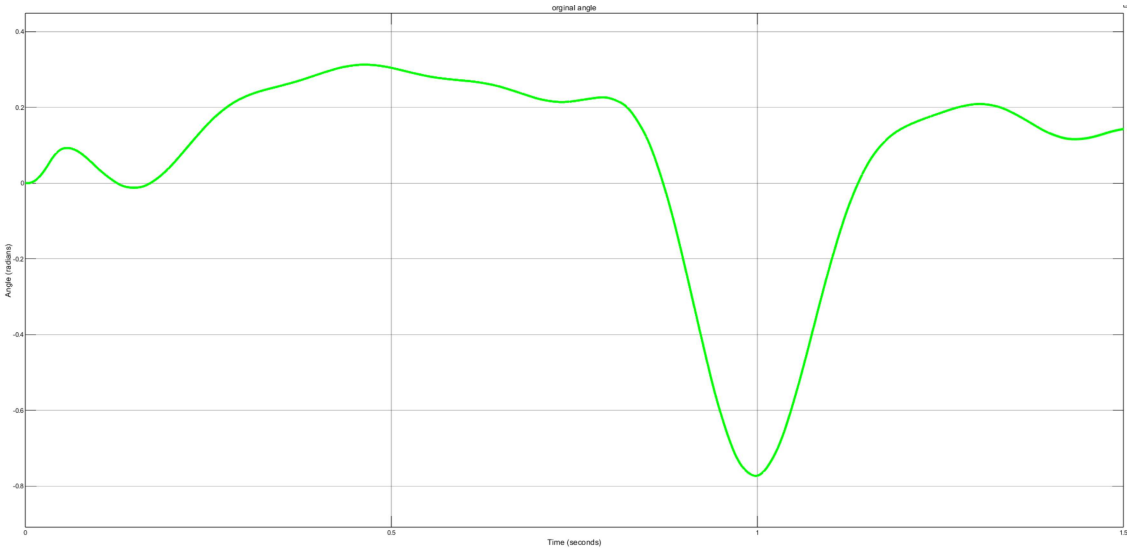

Figure 3.18: Simulation result

3.7 Kinematics

Forward Kinematics

The forward kinematics is used to determine the position and orientation of the foot based on the given joint angle at the input pulley. Based on the motion of the input pulley, the position and orientation of the tip of the foot is calculated. The Denavit-Hartenberg (DH) convention is used to analyze the forward kinematics modeling. Our prostheses have one DOF with belt pulley transmission system, where the actuator rotates the input pulley, transmitting the motion to the output pulley. When joint 1 is rotated by angle $\theta 1$, then joint

2 will rotate by $\theta 1/G$ increasing the torque.

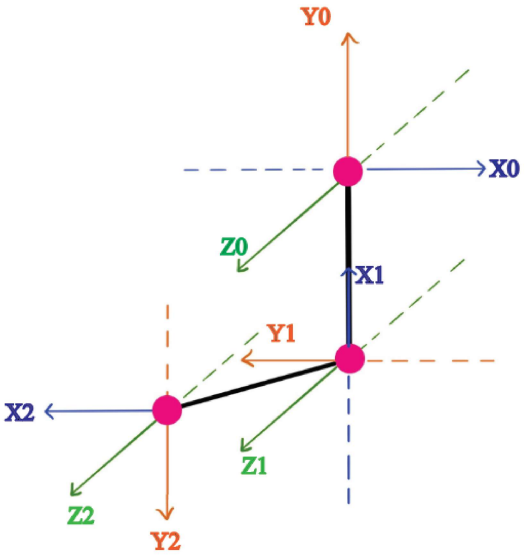

Figure 3.19: FBD showing coordinate system assignment on joint as per DH convention

$$\theta 2 = \theta 1/G \tag{3.78}$$

Table 3.3: DH Table

Link	θ	α	r	d
0-1	$90 + \theta 1$	0	-l1	0
1-2	$90 + \theta 2$	0	l2	0

The transformation matrix obtained is.

$$A_{01} = \begin{bmatrix} -\sin(\theta) & -\cos(\theta) & 0 & -r_1 \sin(\theta) \\ \cos(\theta) & -\sin(\theta) & 0 & r_1 \cos(\theta) \\ 0 & 0 & 1 & 0 \\ 0 & 0 & 0 & 1 \end{bmatrix} \tag{3.79}$$

$$A_{12} = \begin{bmatrix} -\sin\left(\frac{\theta}{G}\right) & -\cos\left(\frac{\theta}{G}\right) & 0 & -r_2\sin\left(\frac{\theta}{G}\right) \\ \cos\left(\frac{\theta}{G}\right) & -\sin\left(\frac{\theta}{G}\right) & 0 & r_2\cos\left(\frac{\theta}{G}\right) \\ 0 & 0 & 1 & 0 \\ 0 & 0 & 0 & 1 \end{bmatrix} \tag{3.80}$$

The transformation matrix of frame 2 concerning base frame is obtained as:

$$T_{0_2} = A_{01} * A_{12} \tag{3.81}$$

The Jacobian matrix is given by

$$J = \begin{bmatrix} R_{00}\begin{bmatrix}0\\0\\1\end{bmatrix}(d_{02}-d_{00}) & R_{01}\begin{bmatrix}0\\0\\1\end{bmatrix}(d_{02}-d_{01}) \\ R_{00}\begin{bmatrix}0\\0\\1\end{bmatrix} & R_{01}\begin{bmatrix}0\\0\\1\end{bmatrix} \end{bmatrix} \tag{3.82}$$

$$J = \begin{bmatrix} -r_1\cos(\theta) + r_2\sin(\theta)\cos\left(\frac{\theta}{G}\right) + r_2\sin\left(\frac{\theta}{G}\right)\cos(\theta) & r_2\sin(\theta)\cos\left(\frac{\theta}{G}\right) + r_2\sin\left(\frac{\theta}{G}\right)\cos(\theta) \\ -r_1\sin(\theta) + r_2\sin(\theta)\sin\left(\frac{\theta}{G}\right) - r_2\cos(\theta)\cos\left(\frac{\theta}{G}\right) & r_2\sin(\theta)\sin\left(\frac{\theta}{G}\right) - r_2\cos(\theta)\cos\left(\frac{\theta}{G}\right) \\ 0 & 0 \\ 0 & 0 \\ 0 & 0 \\ 1 & 1 \end{bmatrix} \tag{3.83}$$

Where R is the rotational matrix obtained from the transformation matrix.

The joint velocity for two joints is given by

$$q = \begin{bmatrix} w_0 \\ w_1 \end{bmatrix} \tag{3.84}$$

The position of the end effector is given by the matrix

$$P = \begin{bmatrix} -r_1 \sin(\theta) + r_2 \sin(\theta) \sin\left(\frac{\theta}{G}\right) - r_2 \cos(\theta) \cos\left(\frac{\theta}{G}\right) \\ r_1 \cos(\theta) - r_2 \sin(\theta) \cos\left(\frac{\theta}{G}\right) - r_2 \sin\left(\frac{\theta}{G}\right) \cos(\theta) \\ 0 \end{bmatrix} \tag{3.85}$$

The velocity vector of the end effector is obtained: v = J * q

$$v = \begin{bmatrix} w_0\big(-r_1 \cos(\theta) + r_2 \sin(\theta) \cos\left(\frac{\theta}{G}\right) + r_2 \sin\left(\frac{\theta}{G}\right) \cos(\theta)\big) \\ +w_1\big(r_2 \sin(\theta) \cos\left(\frac{\theta}{G}\right) + r_2 \sin\left(\frac{\theta}{G}\right) \cos(\theta)\big) \\ w_0\big(-r_1 \sin(\theta) + r_2 \sin(\theta) \sin\left(\frac{\theta}{G}\right) - r_2 \cos(\theta) \cos\left(\frac{\theta}{G}\right)\big) \\ +w_1\big(r_2 \sin(\theta) \sin\left(\frac{\theta}{G}\right) - r_2 \cos(\theta) \cos\left(\frac{\theta}{G}\right)\big) \\ 0 \\ 0 \\ 0 \\ w_0 + w_1 \end{bmatrix}$$

Inverse Kinematics

Inverse Kinematics is used to determine the joint angle when the linear coordinate of the tip of the foot is known. The inverse kinematic is solved analytically through base geometry. The joint angle θ can be calculated as:

$$\theta = \arctan\left(\frac{y_P}{x_P}\right) \tag{3.86}$$

Further details about the simulation process are included here.

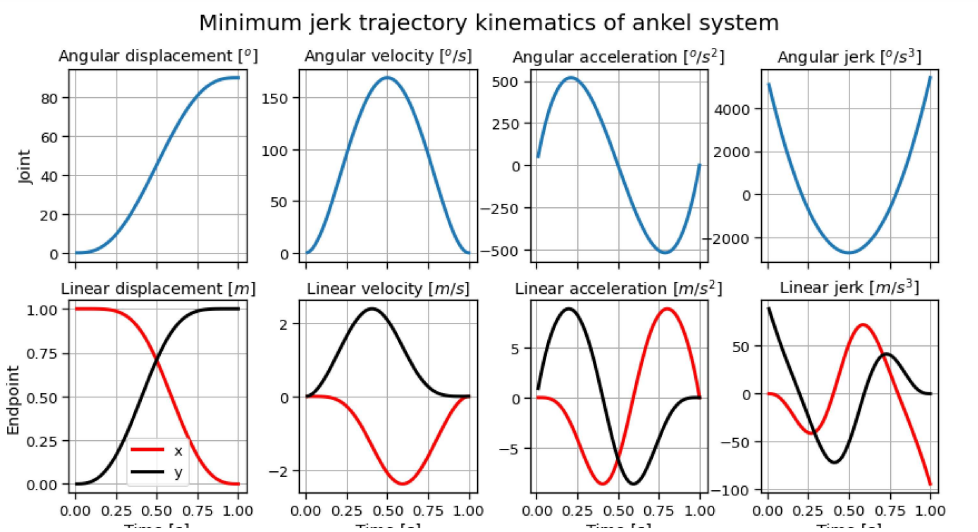

Figure 3.20: Kinematics result

The graph shows a minimum jerk trajectory, which is a smooth and natural motion profile commonly used in biomechanics to simulate natural movements. The smooth transitions in displacement, velocity, acceleration, and jerk indicate that the motion avoids abrupt changes, minimizing energy consumption. Joint and endpoint dynamics are interrelated and correspond to the joint angle.

3.8 Benchtop Testing

Once the structure and control setup of the PAFP were thoroughly tested and analyzed, we moved on to the next phase: Benchtop testing. This stage was crucial for evaluating how the prosthesis would perform in a controlled environment. Below, we outline the tests we conducted on the prosthesis during this phase.

3.8.1 Backdrivability

The backdrivability test was performed to assess the system's compliance, which can be seen in 3.21 and 3.22. The PAFP was rigidly attached to the bench-top setup, allowing the foot to rotate. The motor was not powered during the whole test. Force was then applied at the tip of the foot as in the figure below. A total of 20 trials were performed,

10 each for $+16^\circ$ and -16°. For the case of $+16^\circ$ a downward force was applied to result in plantarflexion and an upward force was applied for -16° for dorsiflexion. During the foot movement, an encoder placed at the output pulley measures the angular velocity($\dot{\omega}$). Angular acceleration($\ddot{\omega}$) is then calculated from this data. Finally, the reflected inertia for the motor, the input pulley in the load (output pulley), and the backdrive torque(τ_b) was calculated.

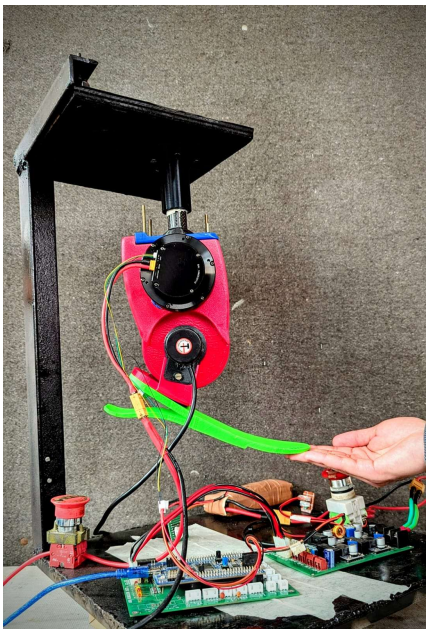

Figure 3.21: Dorsiflexion motion

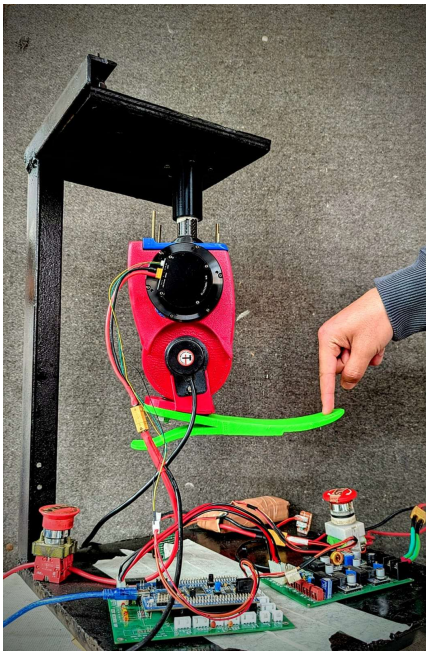

Figure 3.22: Planterflexion motion

3.8.2 Fast Response

The fast response test evaluates the ability of the PAFP to react quickly to heel strikes after the swing phase without toe drag that could lead to tripping or falling. In this test, the prosthetic leg is given an impulse response using a pneumatic system while the motor remains off.

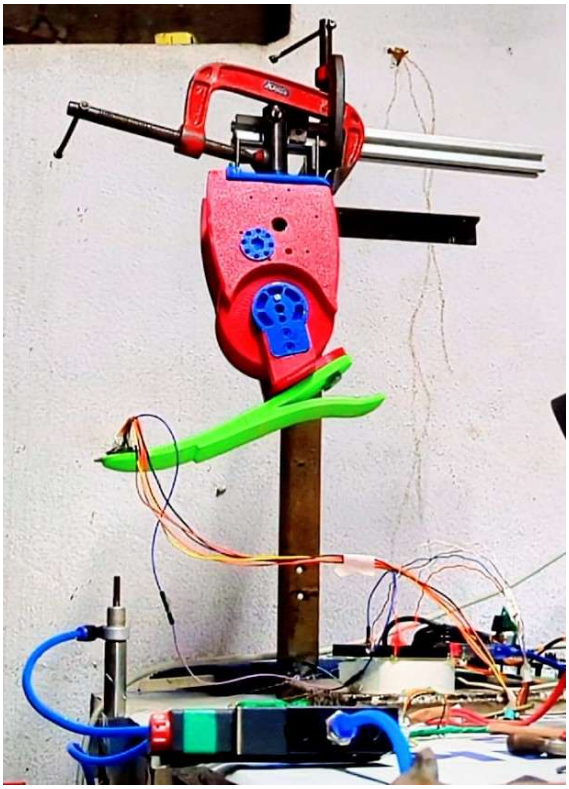

Figure 3.23: Fast Response Test

3.8.3 Loading Test

Loading test was conducted to evaluate the torque-velocity characteristics of the PAFP under biomechanical load conditions. A spring-loaded test bench, with a stiffness of 215 N/m, was used to simulate elastic loading. The test was performed under different loads of 680 g, 1080 g, and 1480 g, representing varying levels of elastic resistance. The ankle was commanded to follow a sinusoidal angular displacement, given by:

$$\theta = \theta_0 sin(\omega t) \tag{3.87}$$

This displacement generated the corresponding output torque, defined as:

$$T_l = -k_l(\theta + \theta_0) \tag{3.88}$$

where,

θ_0 : Equilibrium Point,

ω : Angular Velocity,

k_l : Spring Stiffness

To replicate realistic conditions, the motor applied counter-torque through the angular displacement θ, simulating plantar-flexion under elastic loading and ground reaction forces, similar to the stance of natural walking. During the test, an external encoder recorded the joint's angular velocity ω, an IMU tracked foot position, and the motor's current (A) was continuously monitored to capture its electrical response.

Figure 3.24: Loading Test Setup

The benchtop setup shown in Figure 3.24, the prosthesis was securely mounted on the bench, with a spring of stiffness 215 N/m connected at a distance of 15 cm from the center of the rotary joint. This configuration results in an equivalent torsional stiffness of 4.84 Nm/rad. Since the test was performed with 1480 g load and 4.84 Nm/rad of equivalent torsional stiffness, the target to meet the torque is reduced to 5.068 Nm along with the power of 1.5 W.

CHAPTER 4: RESULT AND DISCUSSION

4.1 Output

The figure 4.1 presents our developed and tested powered ankle-foot prostheses. Initially, the PAFP was designed in SolidWorks, creating the model. The structural analysis was performed in ANSYS to analyze the deformation and stress. Simultaneously, the PAFP was fabricated, and by assembling actuators, encoders, and STM32, the basis of the PAFP was established and tested.

The human gait cycle data was obtained from *Reznick et al.* through which we visualized the normal gait cycle for a human of 80 kg weight, and height of 6 feet 2 inches. The normative ankle angle of the gait cycle was compared with the graph obtained from our PAFP. The backdrivability test was performed to assess the system's compliance and transmission efficiency. Furthermore, a loading test was conducted to evaluate the actuator's capability to produce torque as per the requirement during walking.

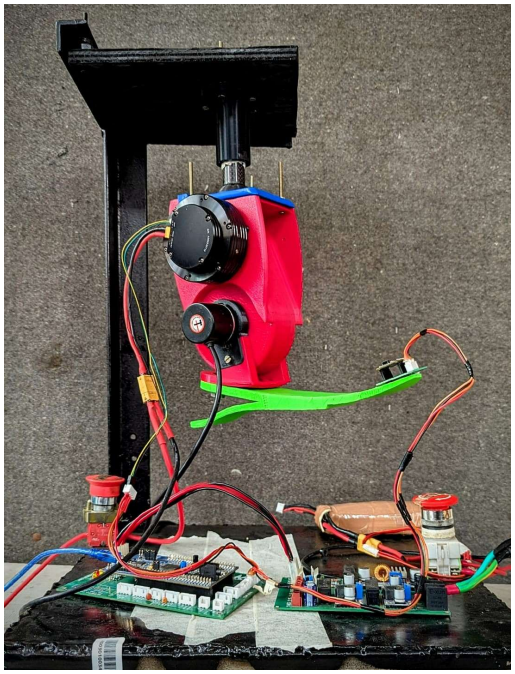

Figure 4.1: Benchtop Setup

4.2 Work Completed

We conducted a series of tests and analyses to validate our benchtop testing. The results we obtained were interpreted while considering resource limitations and the project's scope. We performed multiple trials of the backdrivability test to measure the backdrive torque, as well as a loading test to evaluate the actuator's torque-producing capability and position-tracking performance.

4.2.1 Backdrivability Test

The peak backdrive occurs at the moment when the system's inertia is overcome by the applied force and the pulley starts rotating. The plot of backdrive torque over time reveals the peak values during the test. The magnitude of mean maximum backdrive torque was 2.06 Nmm for dorsiflexion and 2.14 Nmm for plantarflexion. The small torque values prove that the system has low backdrivability. The belt transmission offers an appreciable mechanical efficiency. In addition, the use of lightweight material such as PLA and aluminium for rotating components also resulted in a lower value of the backdrive torque. The result confirms that the system exhibits appreciable backdrivability, as it ensures that the prosthetic can respond naturally to external forces, those encountered during walking.

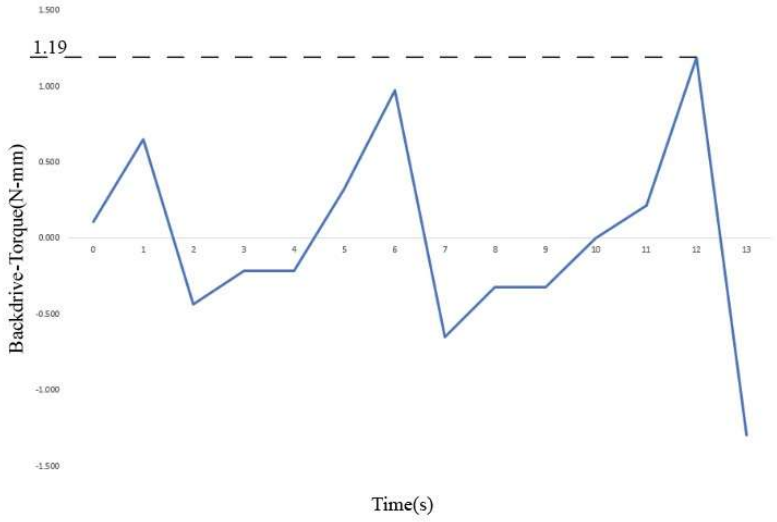

Figure 4.2: Measured Backdrive torque during test

4.2.2 Fast Response Test

The graph in Figure 4.3 illustrates how our system responded to the impulse. From the fast response test, we observed that the PAFP quickly reaches its peak response, indicating a fast reaction to the impulse, with a rise time of less than 1 second. After the initial peak, the angle decays rapidly and stabilizes near the reference angle of 0 degrees. The lack of oscillation indicates good damping, while the small overshoot demonstrates effective controller tuning. The rise time and minimal overshoot showcase the PAFP's capability to track rapid changes in input commands.

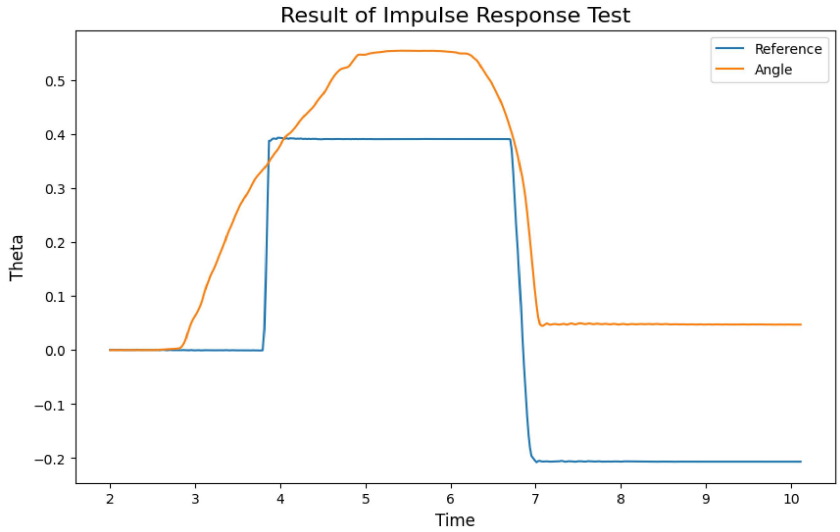

Figure 4.3: Result of Fast Response Test

4.2.3 Loading Test:

The loading test used a spring-loaded bench with a 215 N/m spring placed 15 cm from the joint center, achieving an equivalent torsional stiffness of 4.84 Nm/rad. The prosthesis was driven in a sinusoidal motion under load 1480 g to simulate plantar-flexion. At 1480 g, the system targeted approximately 5.07 Nm torque at 1.5 W power, as confirmed by the encoder, IMU, and motor current data.

1. **Output Current**

   The measured current varies from -0.2 A to about 0.7 A, within the driver's capacity limit of 22 A. The fluctuation trend indicates changes in the current's sign, mainly caused by the motor and system's inertial load.

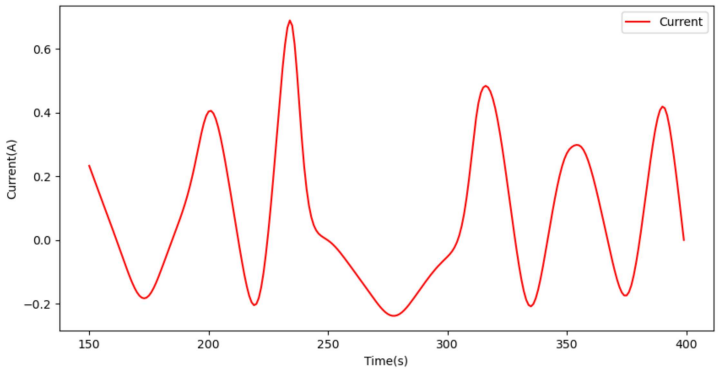

Figure 4.4: Output Current Vs Time

2. **Angular velocity**

   Considering the ankle speed during the human gait cycle ranges from -0.05 rad/s to 0.05 rad/s during plantarflexion and dorsiflexion. This pattern was also replicated by our system during the loading test. Due to errors in the system and sensors, the plot deviates from a sinusoidal shape. Additionally, the presence of inertial force introduces an error of -0.15 rad/s, as shown in Figure 3.8.

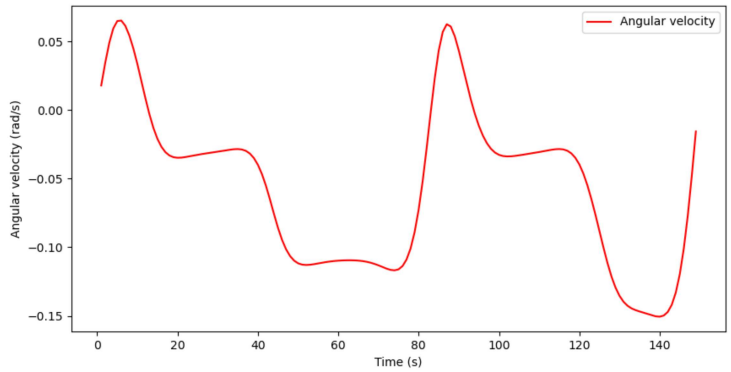

Figure 4.5: Angular velocity(ω) Vs Time(s)

3. **Torque**

The human ankle requires a peak torque of approximately 5.068 Nm for gait, considering a load of 1.48 kg and an equivalent torsional stiffness of 4.84 Nm/rad.The fluctuation trend indicates changes in the torque's sign, mainly caused by the motor and system's inertial load. Under the given test conditions, our system successfully achieved a peak torque of 10 Nm, as illustrated in Figure 34.6, demonstrating a significant improvement over the target requirement.

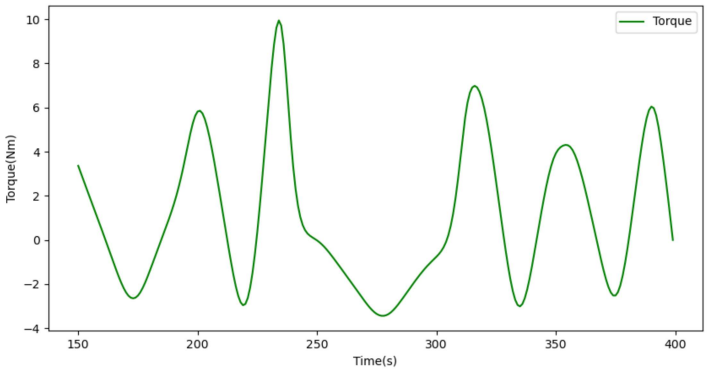

Figure 4.6: Torque Vs Time

4. **Power**

As shown in Figure 4.7, the system's average electrical peak power reaches 0.39 W, which is more than sufficient to generate the required 5.068 Nm torque, significantly exceeding the initial target power of 0.2534 W.Since it's the product of two parameters i.e. torque(τ) and angular velocity(ω), so there is a fluctuation trend indicating changes in the power's direction.

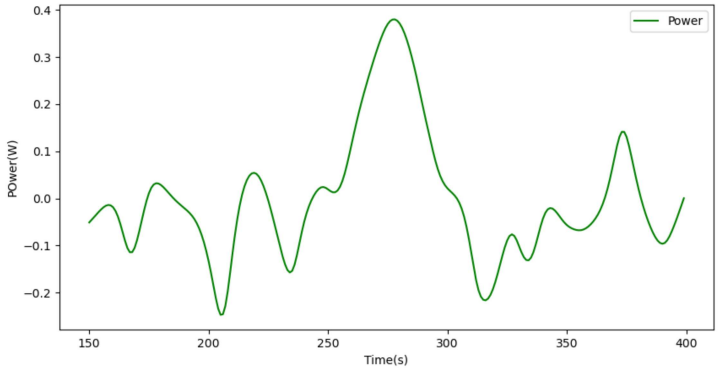

Figure 4.7: Power Vs Time

4.2.4 Position Tracking Validation

After simulating the results, we integrated them into our prosthetic leg to validate the component modeling, control system design, and controller design. This validation is crucial for analyzing our prosthetic leg. We applied the simulated configuration, along with the estimated gain values from the PID controller, to the actual PAFP to collect the gait data. The collected data is plotted as shown in Figure 4.8

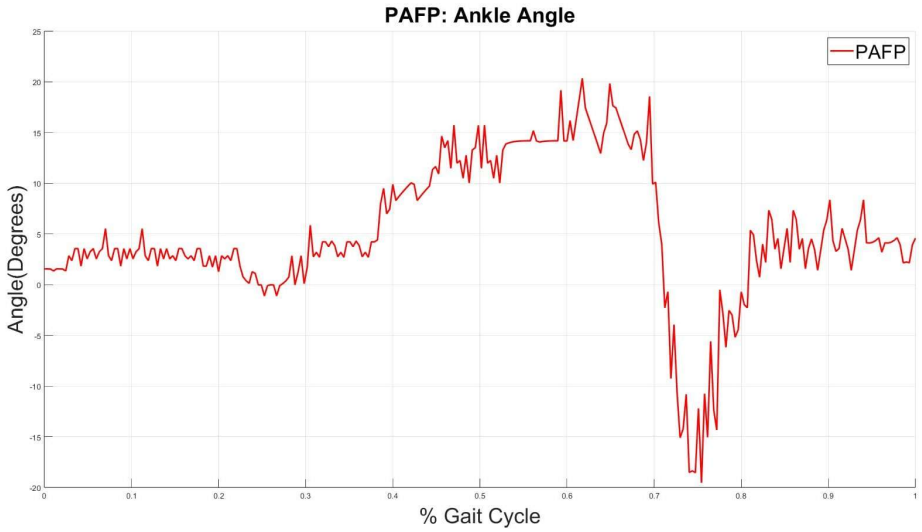

Figure 4.8: Angle vs % Gait plot of PAFP

The gait cycle graph obtained from our PAFP differs from the normal gait cycle due to delays and oscillation as shown in Figure 4.8.

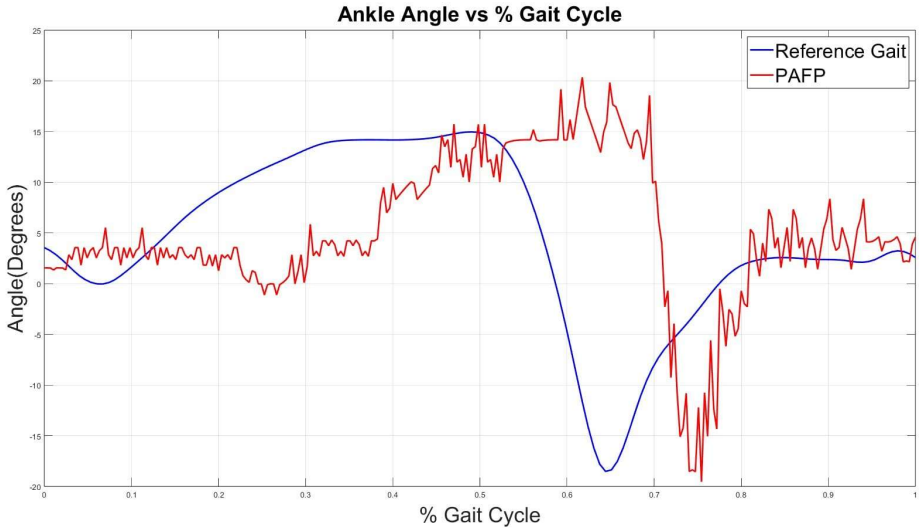

Figure 4.9: Angle plot comparison of PAFP with reference gait over a stride

From the graph 4.9, we observed a delay in the time response, which we identified as being caused by the actuator's response time. We conducted a step response test on the motor, focusing on the overshoot and settling time required to reach the desired setpoint. Based on the insights gained from this analysis, we adjusted the tuning of the PID controller, resulting in a significant improvement in the alignment between the robot's performance and the gait data, as shown in the graph 4.10. There is still some detail in the gait phase which can be solved with further tuning of the PID and use of the CAN communication protocol instead of UART communication protocol.

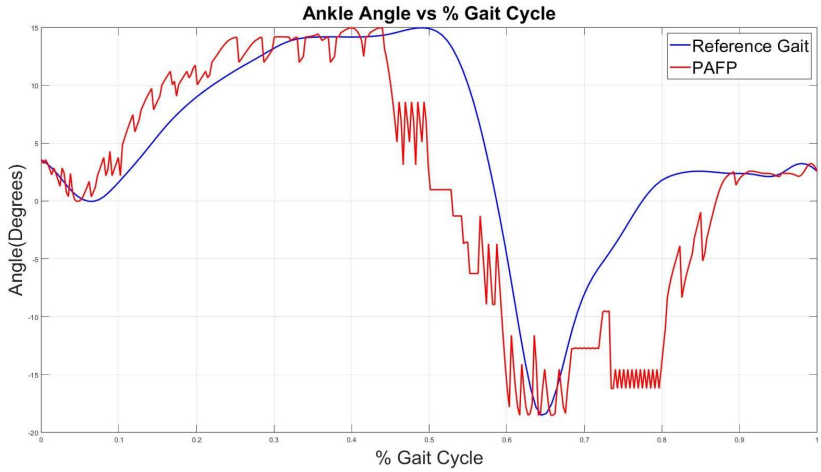

Figure 4.10: Result after PID Tuning

Adjusting the PID controller helped mitigate the issue of time delay, but there was still noise present in the raw data collected from the IMU. To reduce the high-frequency noise and better capture the true response of the system, a Butterworth low-pass filter was applied. This significantly improved the result of the gait cycle, as illustrated in the graph 4.11.

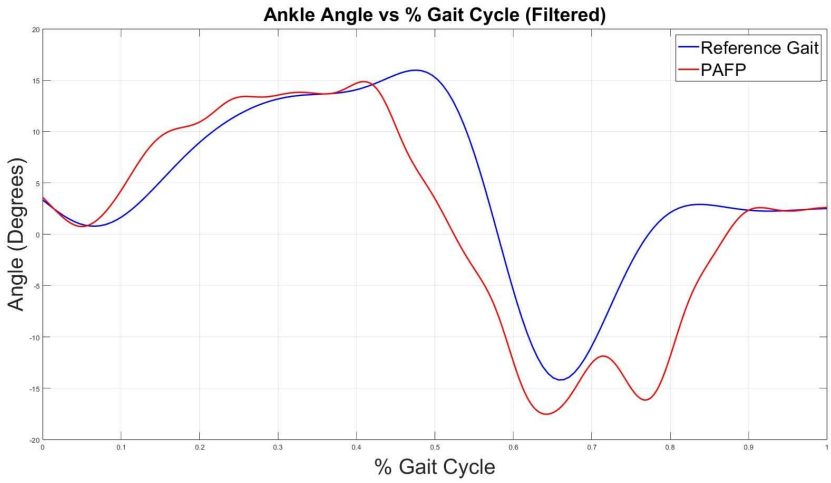

Figure 4.11: Result after Butterworth filter application

4.2.5 Structural Analysis

A structural analysis of the input and output pulley system was performed using ANSYS to evaluate total deformation and equivalent stress under peak torque conditions to analyze whether it can withstand the peak torque. The results are detailed below.

1. **Input Pulley:** We conducted the structural analysis in ANSYS for the input pulley to see the deformation and equivalent stress assuming only torque is applied to the driving portion of the input pulley.

   (a) Total Deformation: The maximum total deformation in the input pulley was evaluated to be 2.7023×10^{-5} m which is negligible compared to the dimensions of the input pulley.

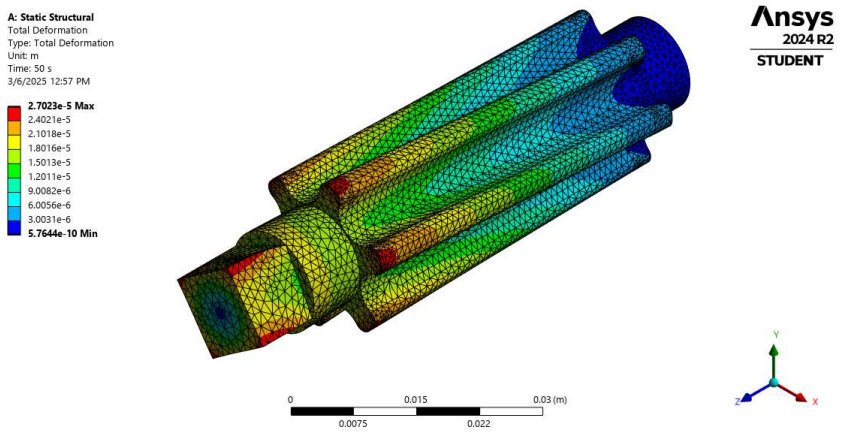

Figure 4.12: Total Deformation of Input Pulley

   (b) Equivalent Stress: The generated equivalent stress in the input pulley is 60.687 MPa, which is less than the endurance limit of 119.7 MPa, indicating we can run this system at about 9 Nm, which is 4 times the operating region before its failure.

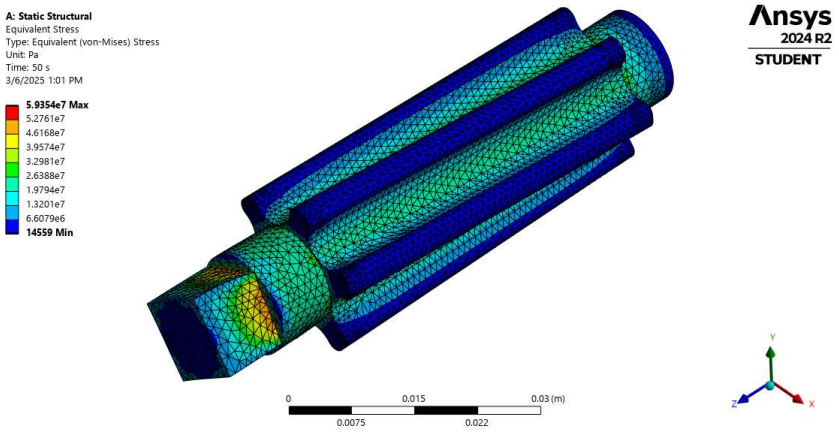

Figure 4.13: Equivalent Stress on Input Pulley

2. **Output Pulley system:** We conducted the structural analysis in ANSYS for the output pulley system to see the deformation and equivalent stress assuming only torque is applied to the driven portion of the output pulley profile.

   (a) Total Deformation: Through the analysis in ANSYS, the total deformation generated in the output pulley was evaluated to be 1.1324×10^{-3}m.

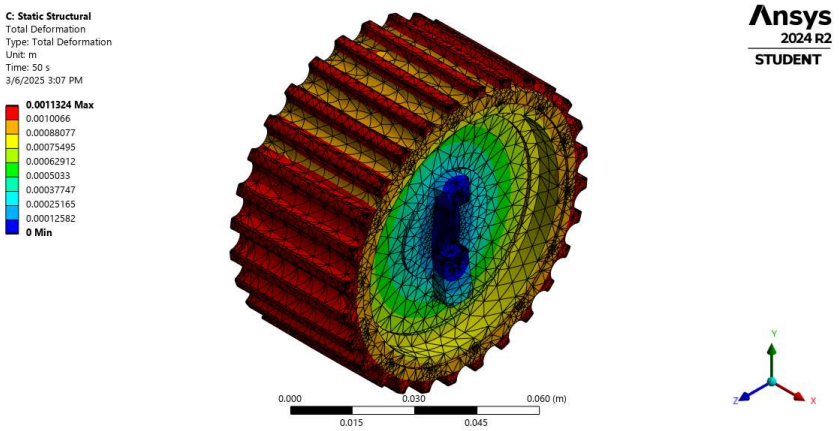

Figure 4.14: Total Deformation of Output Pulley

   (b) Von Mises Stress (Equivalent Stress): The equivalent stress in output pulley system was evaluated to be 62.71 MPa.

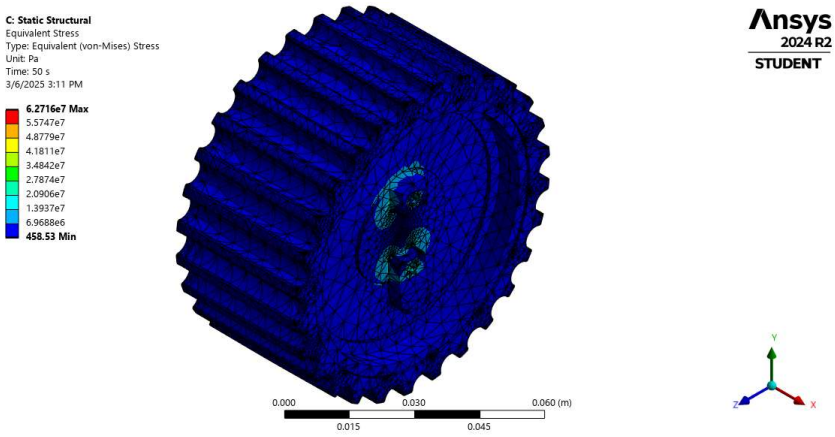

Figure 4.15: Equivalent Stress on Output Pulley

4.3 Limitations

1. **Communication Delays:** The communication delay in our project has limited real-time responsiveness. This latency may be caused by the serial data handling of the UART communication protocol. Additionally, unoptimized code has increased computational time and slowed down the response.

2. **Motion Constraint:** The project focuses mainly on the ankle movement to the sagittal plane for walking at 1 m/s speed only and has not studied the dynamic activities like running, uneven terrains and rapid direction changes. The analysis of gait dynamics in the frontal and transverse planes is not studied, which is essential for real human locomotion.

3. **Clinical Validation:** The benchtop testing has validated the control and mechanical performance of the prosthesis. However, it lacks clinical testing and validation with human subjects for real-world implementation.

4.4 Problem Faced

1. **Mechanical Failure:**

   The input pulley experiences high torque from the motor, which the 3D printed pulley

could not withstand, leading to repeated breakage. The breakage may be due to improper printing and stress concentration at critical points. To mitigate this issue, we machined the input pulley using Aluminum.

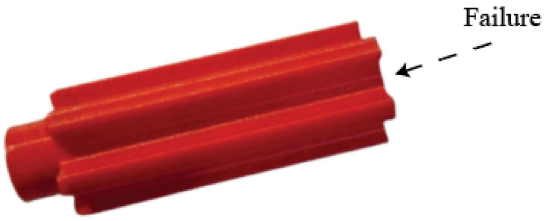

Figure 4.16: Input Pulley Failure

2. **Communication Issues:**

   The setup of UART communication among the motor and controller required extensive coding and error handling to develop libraries for each sensor, such as IMU, encoder. The process demanded considerable time and effort to ensure accurate functionality.

3. **Motor:**

   Initially, we used a BLDC motor as the actuator for our project; however, it did not meet our torque requirements. Consequently, we had to temporarily halt progress until we received the AK60-6 motor from CubeMars, which met our torque and speed control needs. With the new motor in place, we were able to resume work and continue the development as planned.

4. **PID Tuning:**

   The PID controller was not tuned initially, which led to difficulties during the position tracking test. We experienced high oscillations in the data, making it challenging to achieve a stable and accurate gait pattern. After applying the root locus method to tune the gain parameters, we were able to obtain smoother data.

CHAPTER 5: CONCLUSION AND FUTURE ENHANCEMENT

This thesis presents the achievements of the project, highlighting the final outcomes, methodolgy used to conduct and, validate experiments, and challenges faced at every stage. The final prototype has been fully fabricated, with motor, controller and sensors integrated with UART communication protocol and PID implementation.

The structural analysis of the input pulley and output pulley in ANSYS helped in refining the final design of the PAFP. Mathematical modeling and Simulink model aided in understanding the system's response. Kinematics and dynamic modeling helped in validating mechanical response of the prosthesis. Benchtop testing demonstrated the PAFP's compliance, load response, and position tracking ability, which was comparable to normal gait trajectories. Throughout the development, multiple issues from resource limitations, component failures, hardware malfunction, and debugging issues were encountered. Despite all these issues, we successfully achieved targeted objectives of the project. Hence, this project aims to make a valuable contribution to the field of prosthetic design and development.

The prototypes developed have undergone benchtop testing only. Further advancements and improvements can be made for use in real-world activities. The following future works can be considered:

1. The PAFP can be fabricated using more durable and biocompatible materials to perform tests on human subjects while evaluating dynamic walking conditions.

2. Current PAFP has undergone benchtop testing for walking only, but it can be further improved for activities like running, stair climbing, and walking on uneven terrains.

3. The PAFP can integrate advanced sensors like EMG, load cells, and pressure sensors to enhance real-time motion tracking and adaptive gait control.

4. Machine learning algorithms can be implemented to adapt to the different walking patterns based on the user's gait and predict the prosthetic movement.

5. Switching from the UART communication protocol to the CAN protocol can improve data transmission speed and efficiency, reducing response time delays. Incorporating a high-energy-density battery will also enhance power availability, extending the operational time. Additionally, using a more advanced and compact processor can further optimize system performance.

REFERENCES

1 B. Yuan, D. Hu, S. Gu, S. Xiao, and F. Song, "The global burden of traumatic amputation in 204 countries and territories," *Frontiers in public health*, vol. 11, p. 1 258 853, 2023.

2 K. A. Raichle, M. A. Hanley, I. Molton, *et al.*, "Prosthesis use in persons with lower- and upper-limb amputation," *Journal of rehabilitation research and development*, vol. 45, no. 7, p. 961, 2008.

3 C. Prasanna, J. Realmuto, A. Anderson, E. Rombokas, and G. Klute, "A data-driven and personalized stance symmetry controller for robotic ankle-foot prostheses: A preliminary investigation," *IEEE Transactions on Neural Systems and Rehabilitation Engineering*, vol. 31, pp. 4051–4062, 2023.

4 F. Sup, A. Bohara, and M. Goldfarb, "Design and control of a powered transfemoral prosthesis," *The International journal of robotics research*, vol. 27, no. 2, pp. 263–273, 2008.

5 Y. CHEN, B. XUAN1, Y. GENG1, S. DING, and L. CHEN, "Modeling and control of knee-ankle-toe active transfemoral prosthesis," *IEEE Access*, 2020.

6 T. Elery, S. Rezazadeh, E. Reznick, L. Gray, and R. D. Gregg, "Effects of a powered knee-ankle prosthesis on amputee hip compensations: A case series," *IEEE Transactions on Neural Systems and Rehabilitation Engineering*, vol. 28, pp. 1234–1243, 2020.

7 Y. Zeng, "Design and testing of a passive prosthetic ankle with mechanical performance similar to that of a natural ankle," 2013.

8 T. Elery, S. Rezazadeh, C. Nesler, J. Doan, H. Zhu, and R. D. Gregg, "Design and benchtop validation of a powered knee-ankle prosthesis with high-torque, low-impedance actuators," in *2018 IEEE international conference on robotics and automation (ICRA)*, IEEE, 2018, pp. 2788–2795.

9 M. Cempini, L. J. Hargrove, and T. Lenzi, "Design, development, and bench-top testing of a powered polycentric ankle prosthesis," in *2017 IEEE/RSJ International Conference on Intelligent Robots and Systems (IROS)*, IEEE, 2017, pp. 1064–1069.

10 A. Saboor, T. Kask, A. Kuusik, *et al.*, “Latest research trends in gait analysis using wearable sensors and machine learning: A systematic review,” *Ieee Access*, vol. 8, pp. 167 830–167 864, 2020.

11 M. Asif, M. A. Tayyab, M. H. Shahid, *et al.*, “Analysis of human gait cycle with body equilibrium based on leg orientation,” *IEEE Access*, vol. 10, pp. 123 177–123 189, 2022.

12 E. Reznick, K. R. Embry, R. Neuman, E. Bolívar-Nieto, N. P. Fey, and R. D. Gregg, “Lower-limb kinematics and kinetics during continuously varying human locomotion,” *Scientific Data*, vol. 8, no. 1, p. 282, 2021.

13 T. Elery, S. Rezazadeh, C. Nesler, and R. D. Gregg, “Design and validation of a powered knee–ankle prosthesis with high-torque, low-impedance actuators,” *IEEE Transactions on Robotics*, pp. 1649–1668, 2020.

14 ". Kenji", “"material selection of below-knee leg prosthetics",” *"journal of Materials Exploration and Findings (JMEF)"*, "August, 15 2022".

15 T. Sarma, D. Pandey, N. Sahai, and R. P. Tewari, “Material selection and development of ankle foot orthotic device,” *Materials Today: Proceedings*, vol. 18, pp. 2509–2514, 2019.

16 D. S. Pieringer, M. Grimmer, M. F. Russold, and R. Riener, “Review of the actuators of active knee prostheses and their target design outputs for activities of daily living,” in *2017 International Conference on Rehabilitation Robotics (ICORR)*, IEEE, 2017, pp. 1246–1253.

17 B. G. Katz, “A low cost modular actuator for dynamic robots,” Ph.D. dissertation, Massachusetts Institute of Technology, 2018.

18 R. Gehlhar, “Model-based lower-limb powered prosthesis control: Developing and realizing nonlinear subsystem control methods for generalizable prosthesis control,” Available at https://resolver.caltech.edu/CaltechTHESIS:01072023-214003146, PhD thesis, CALIFORNIA INSTITUTE OF TECHNOLOGY, Pasadena, California, Dec. 2022.

19 P. L. Garcia, E. Saerens, S. Crispel, A. Varadharajan, D. Lefeber, and T. Verstraten, "Factors influencing actuator's backdrivability in human-centered robotics," in *MATEC Web of Conferences*, EDP Sciences, vol. 366, 2022, p. 01 002.

20 H. O. Bansal, R. Sharma, and P. Shreeraman, "PID controller tuning techniques: A review," *J. Control Eng. Technol*, vol. 2, no. 4, pp. 168–176, 2012.

21 J. W. Grizzle, G. Abba, and F. Plestan, "Asymptotically stable walking for biped robots: Analysis via systems with impulse effects," *IEEE Transactions on Automatic Control*, vol. 46, no. 1, pp. 51–64, 2001.

22 A. Martin and R. D. Gregg, "Stable, robust hybrid zero dynamics control of powered lower-limb prostheses," *IEEE Trans. Automatic Control*, vol. 62, no. 8, pp. 3930–3942, 2017.

23 K. Shamaei, G. S. Sawicki, and A. M. Dollar, "Estimation of quasi-stiffness of the human knee in the stance phase of walking," *PloS one*, vol. 8, no. 3, e59993, 2013.

24 Y. H. C. Man Lok Fung Michael Z. Q. Chen, "Sensor fusion: A review of methods and applications," *29th Chinese Control And Decision Conference (CCDC)*, 2017.

25 R. E. Kalman, "A New Approach to Linear Filtering and Prediction Problems," *Transactions of the ASME–Journal of Basic Engineering*, vol. 82, no. Series D, pp. 35–45, 1960.

26 *Extended Kalman filter*, en, Page Version ID: 1185257110, Nov. 2023. [Online]. Available: https://en.wikipedia.org/w/index.php?title=Extended_Kalman_filter&oldid=1185257110 (visited on 12/20/2023).

27 E. Wan and R. Van Der Merwe, "The unscented Kalman filter for nonlinear estimation," in *Proceedings of the IEEE 2000 Adaptive Systems for Signal Processing, Communications, and Control Symposium (Cat. No.00EX373)*, Oct. 2000, pp. 153–158. DOI: 10.1109/ASSPCC.2000.882463. [Online]. Available: https://ieeexplore.ieee.org/document/882463 (visited on 12/19/2023).

28 P. L. Garcia, E. Saerens, S. Crispel, A. Varadharajan, D. Lefeber, and T. Verstraten, "Factors influencing actuator's backdrivability in human-centered robotics," in *MATEC Web of Conferences*, EDP Sciences, vol. 366, 2022, p. 01 002.

29 B. L. "Qitao Huang and H. Xu", “"the design and testing of a pea powered ankle prosthesis driven by eha",” *"biomimetics"*, 2022.

30 N. Muruganantham and S. Palani, “State space modeling and simulation of sensorless permanent magnet bldc motor,” *International Journal of Engineering Science and Technology*, vol. 2, no. 10, pp. 5099–5106, 2010.

APPENDIX A

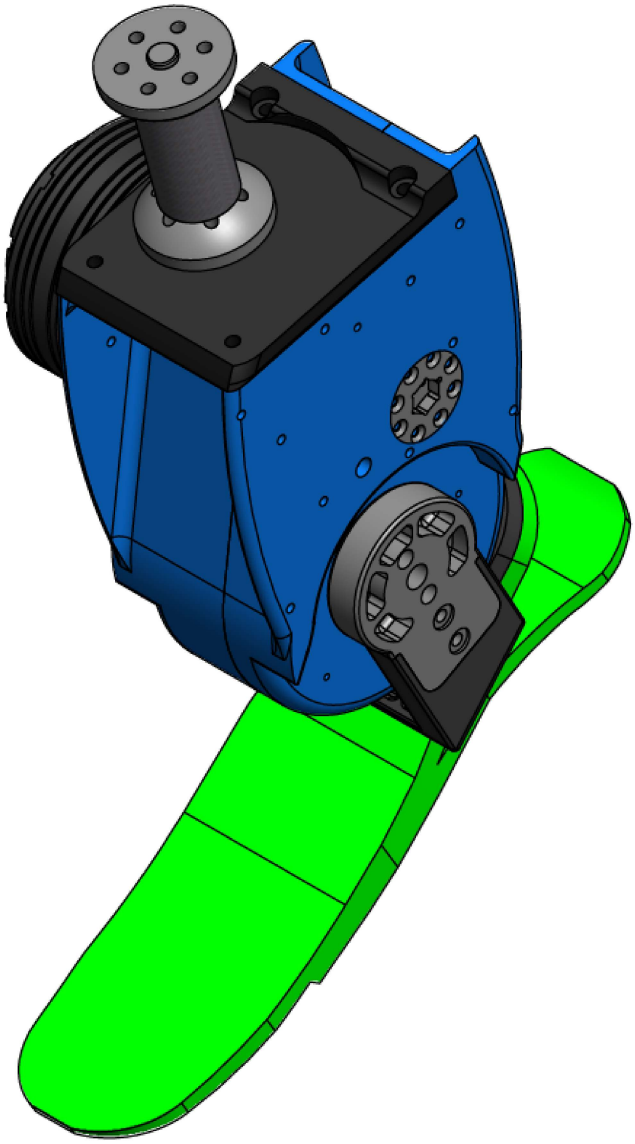

Figure A1: Ankle Foot Prosthesis Assembly

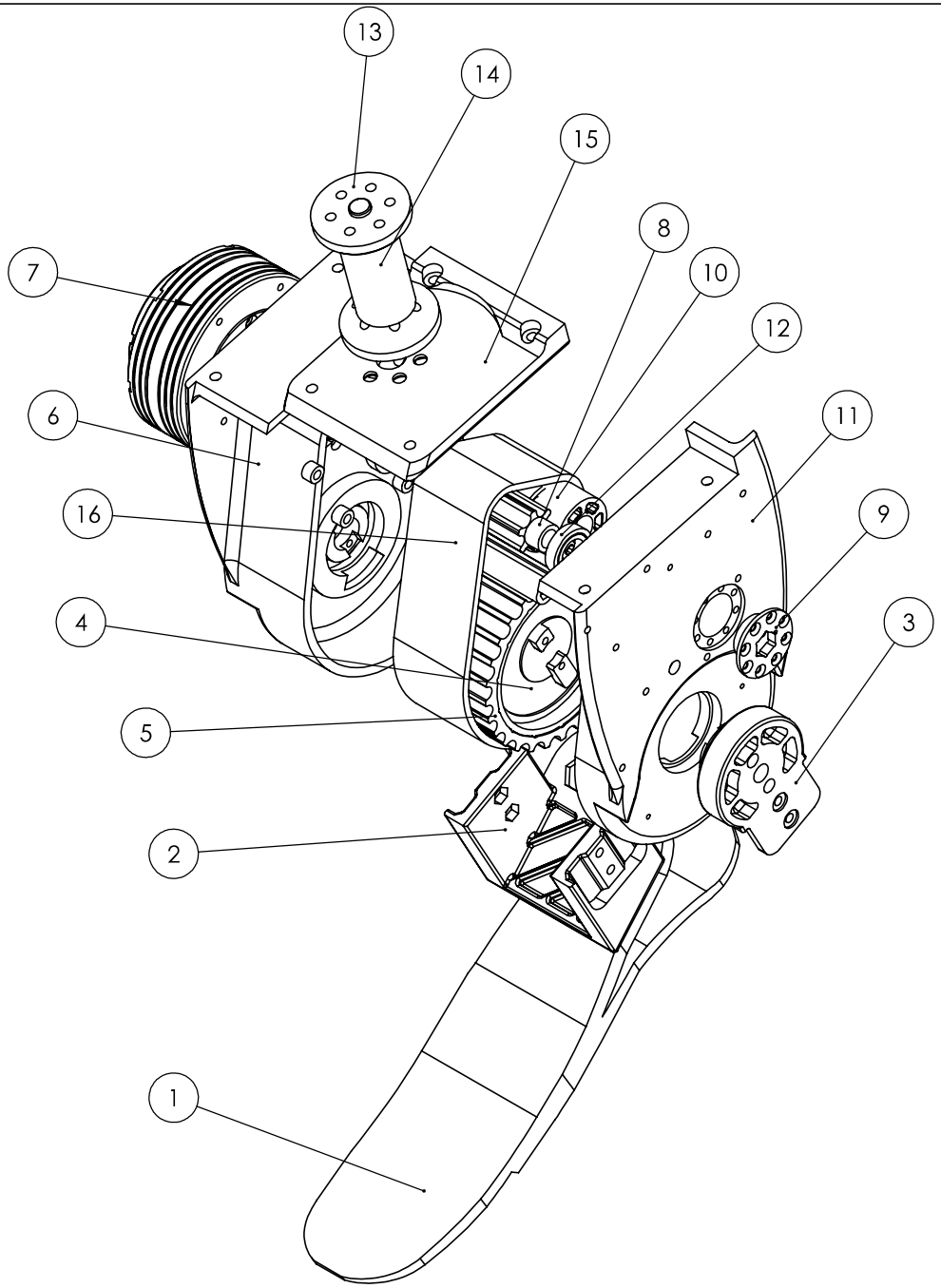

ITEM NO.	COMPONENT	QTY.
1	Asthetic Foot	1
2	Pyramid Veriflex	1
3	Pyramid Strut	2
4	Gear Stop	2
5	Ouput Pulley	1
6	Ankle Housing Right	1
7	Actuator	1
8	Input Pulley	1
9	Shaft Capc Eccentric	3
10	Idler Shell	1
11	Ankle Housing Left	1
12	Bearing	2
13	Leg Pylon Coupler	2
14	Pylon	1
15	Top Base	1
16	Belt	1

Title: Powered Ankle Foot Prostheses Assembly	
Scale: 1:2	Sheet No.: 1

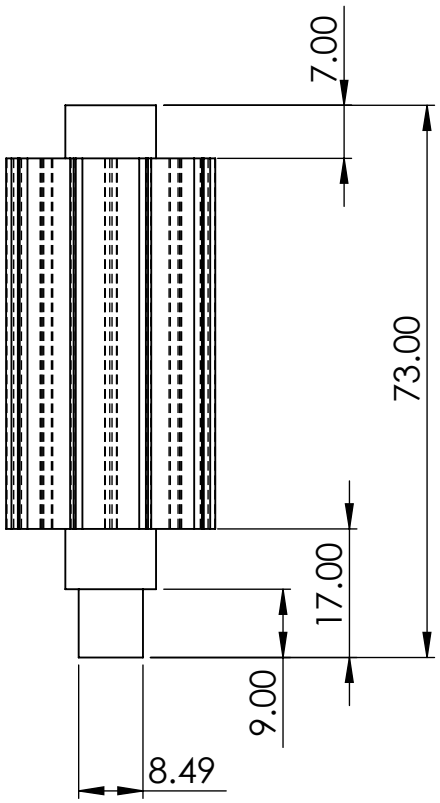

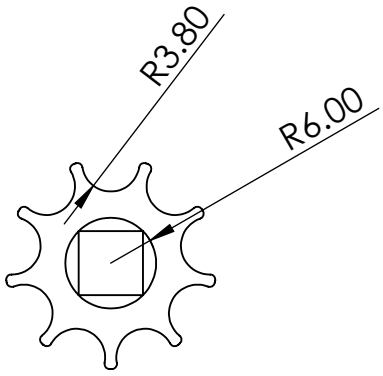

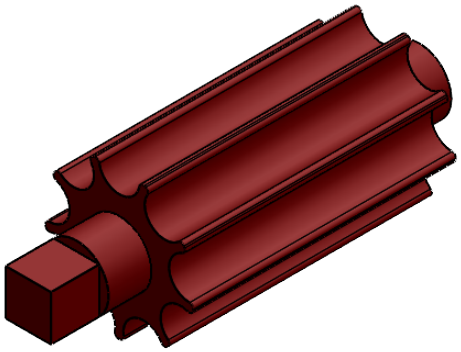

TITLE: Input Pulley		
Scale: 1:1	Material: Aluminium	Sheet No.: 2
	Unit: mm	

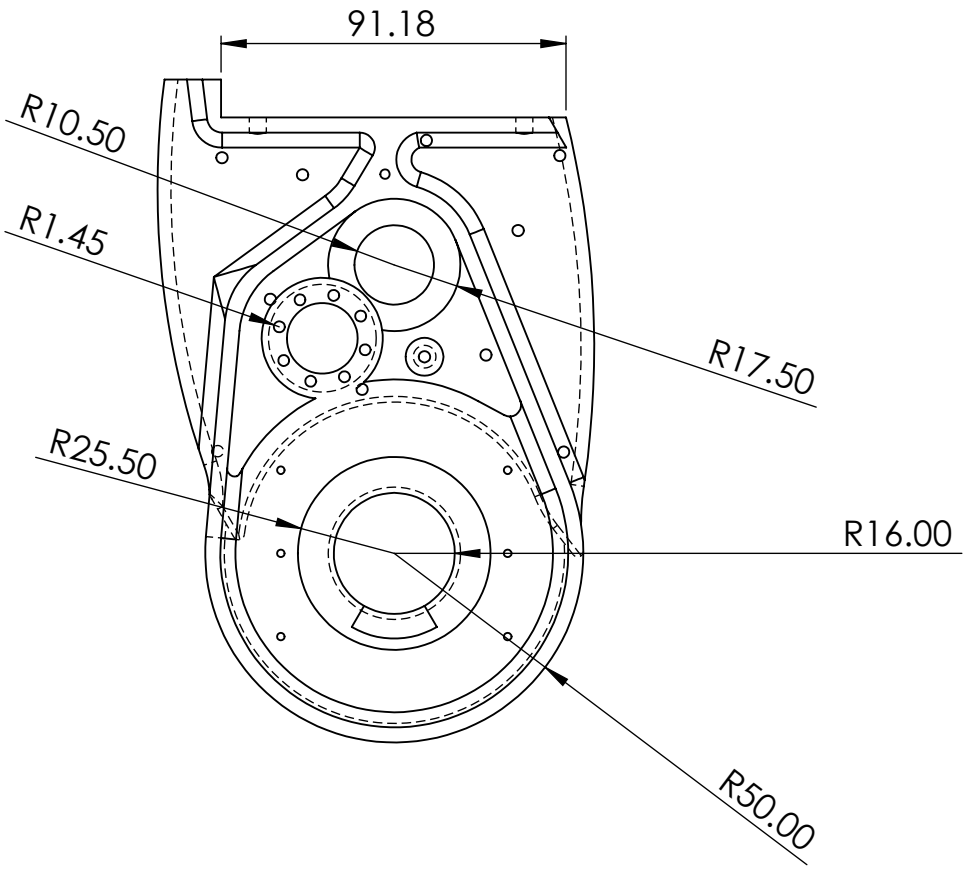

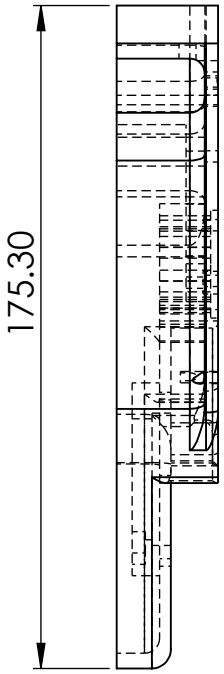

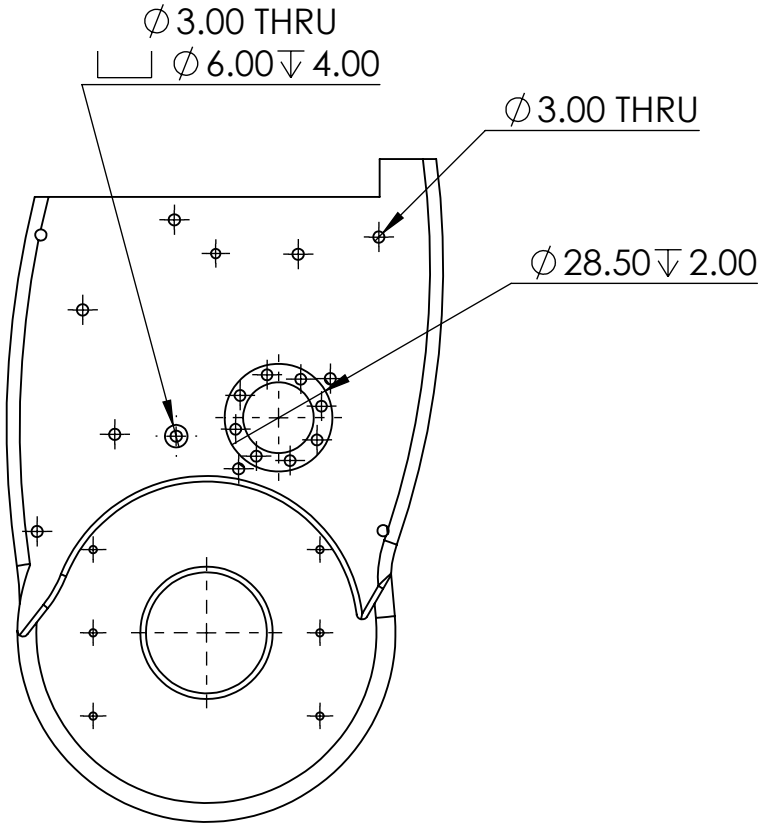

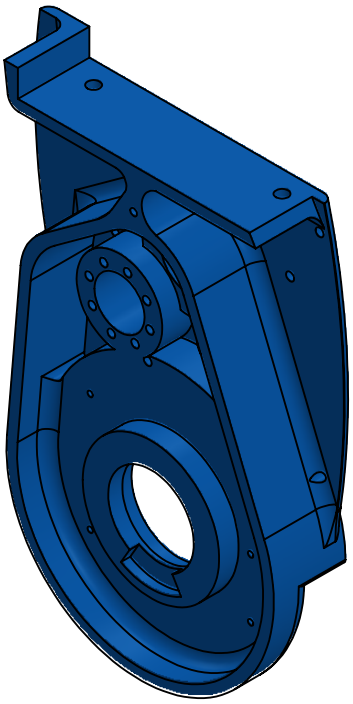

Title: Ankle Housing Left		
	Material: PLA	Scale: 1:2
	Units: mm	Sheet No.: 3

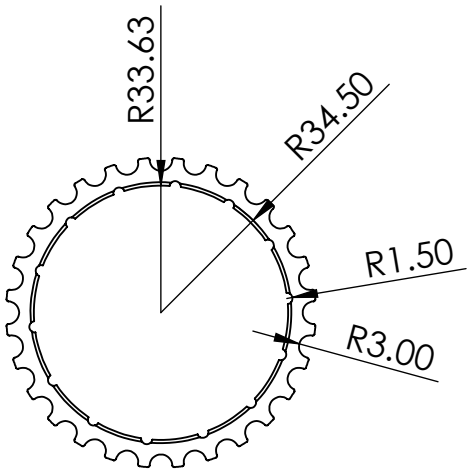

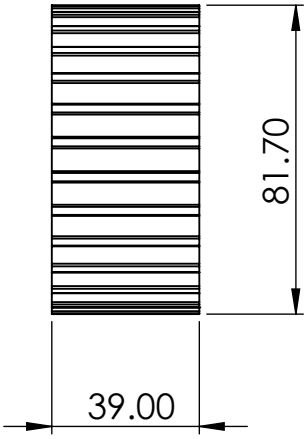

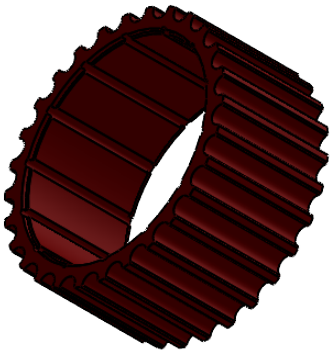

Title: Output Pulley		
	Material: PLA	Scale: 1:2
	Unit: mm	Sheet No.: 4

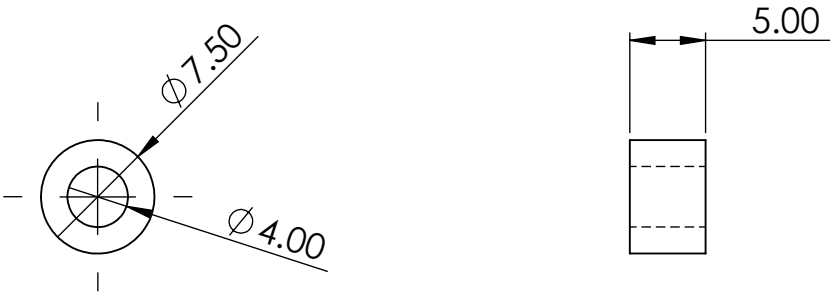

Actuator Spacer

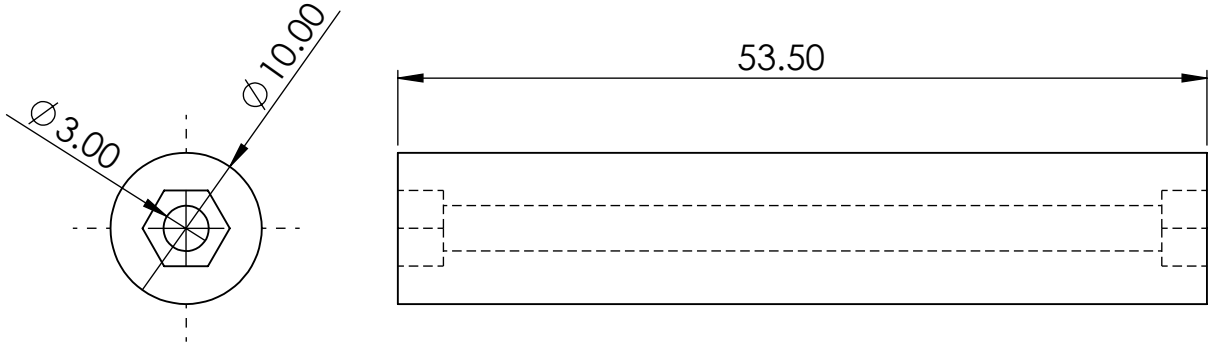

Connector

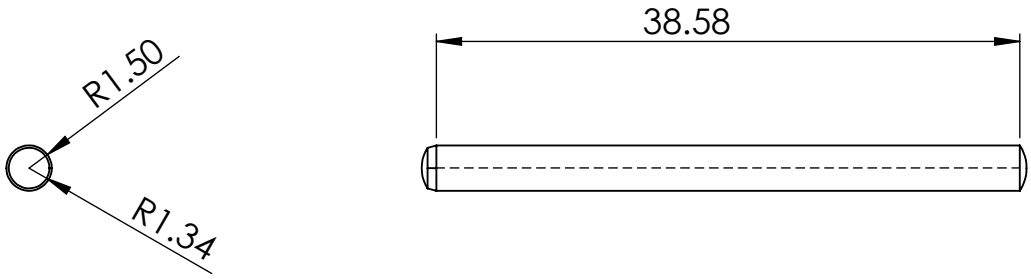

Idler Shaft

	Material: PLA	Scale: 5:1
	Unit: mm	Sheet No.: 5

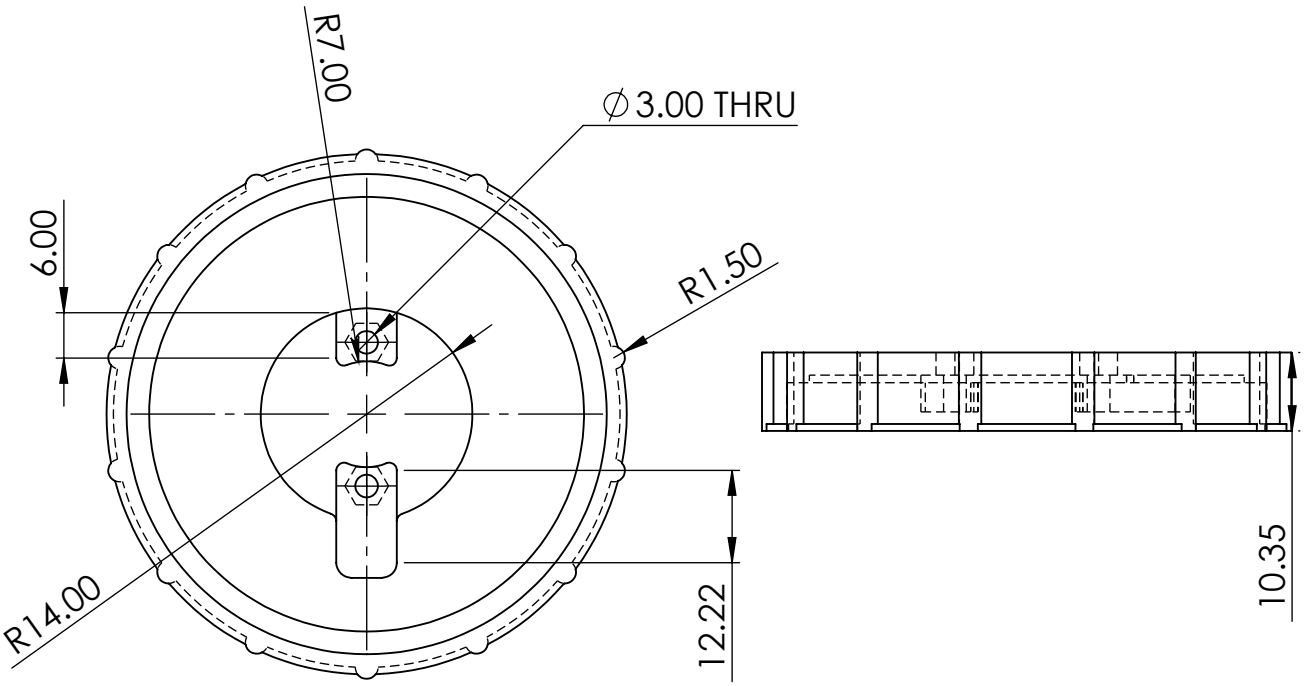

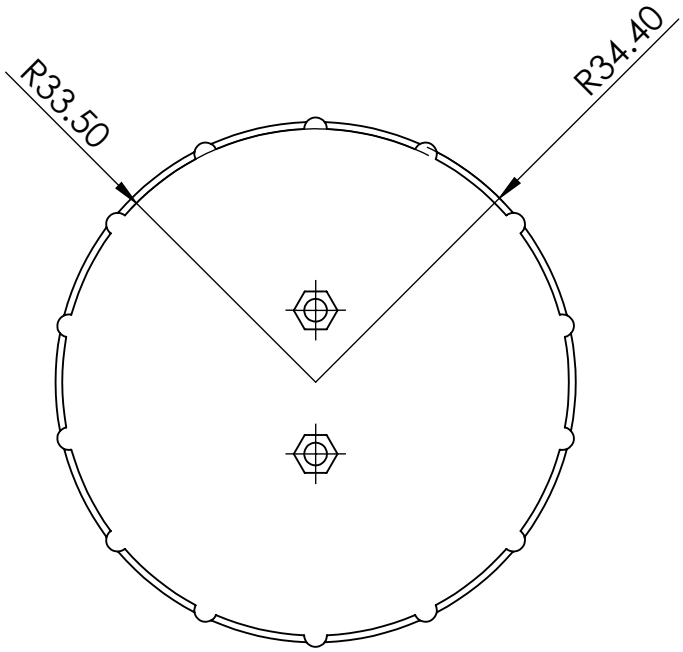

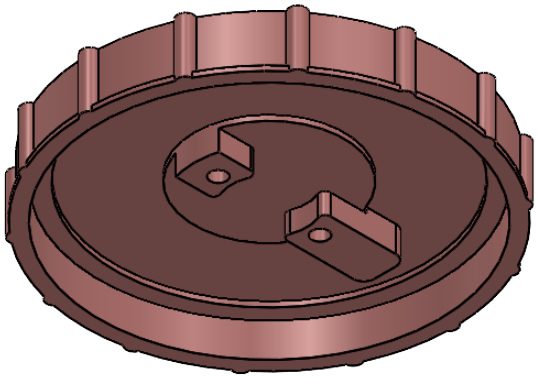

Title: Gear Stop		
	Material: PLA	Scale: 1:2
	Unit: mm	Sheet No.: 6

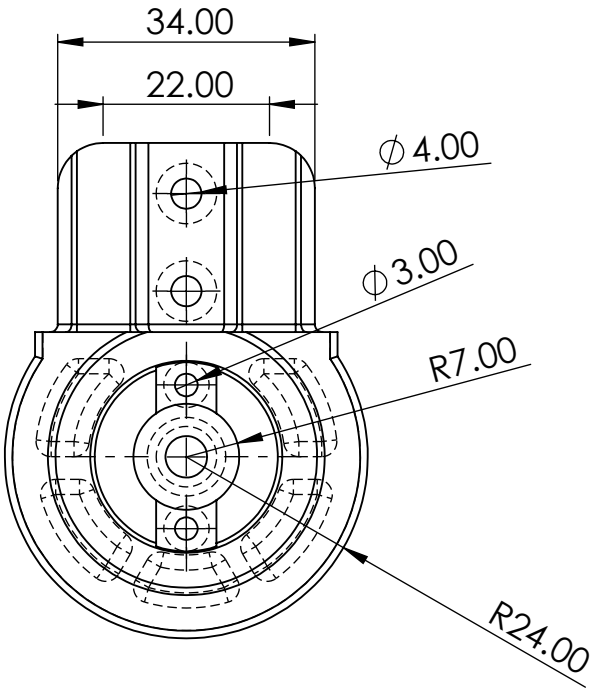

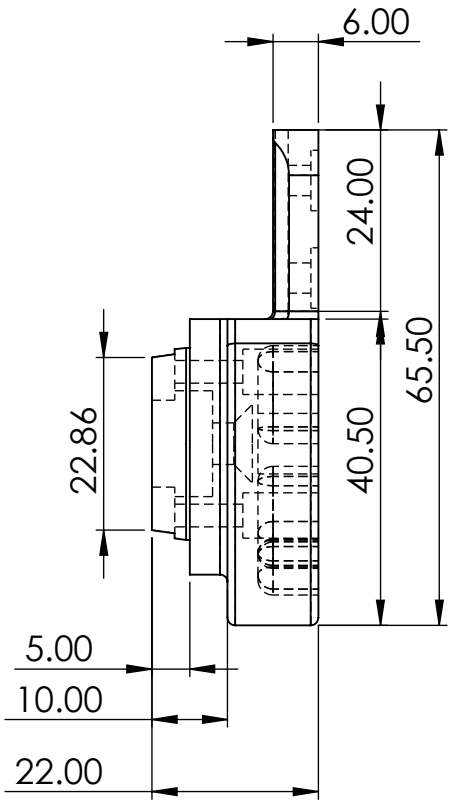

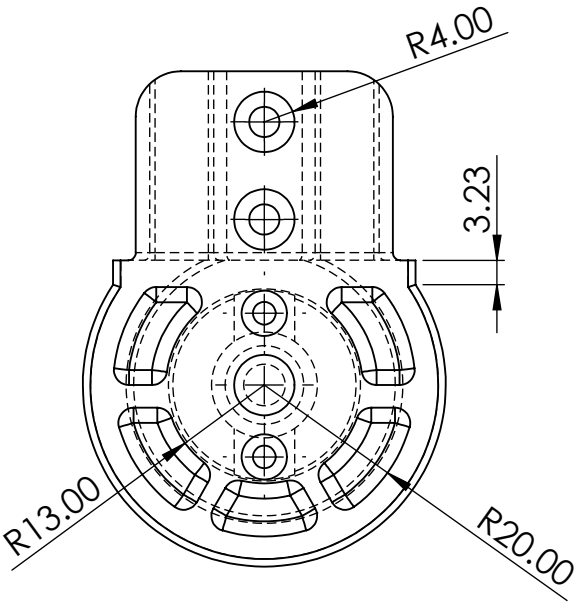

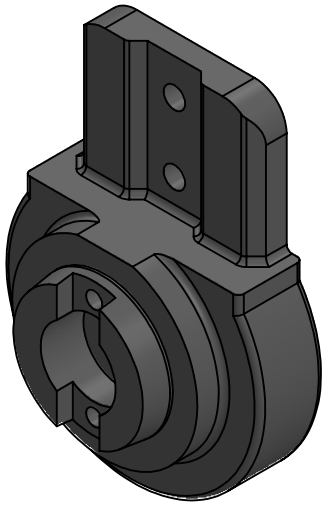

Title: Pyramid Strut		
	Material: PLA	Scale: 1:1
	Unit: mm	Sheet No.: 7

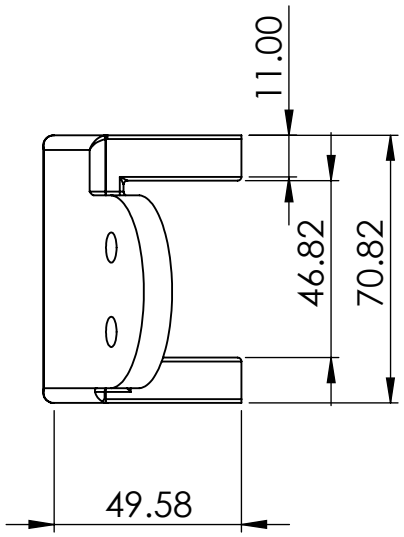

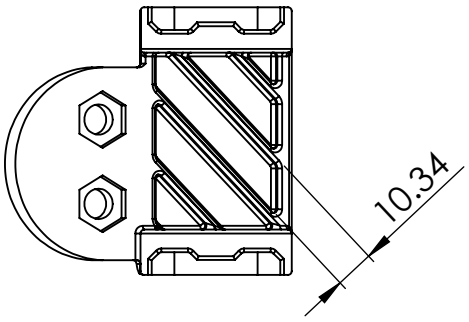

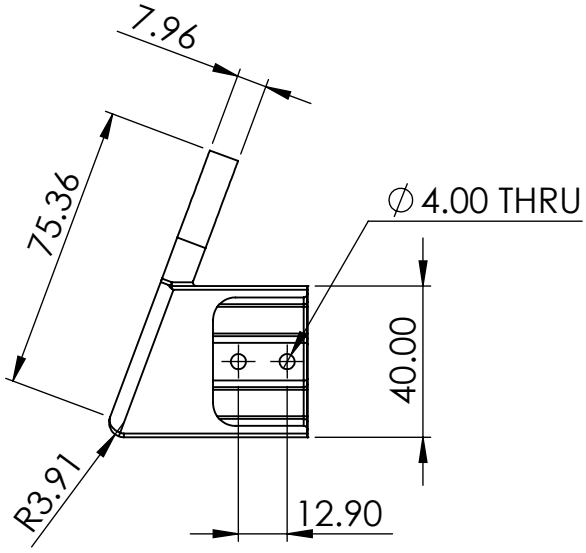

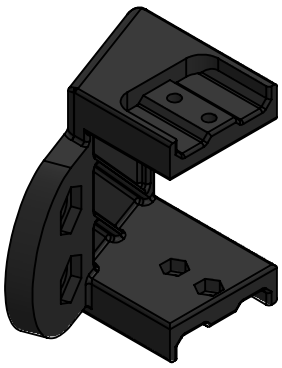

Title: Pyramid Veriflex		
	Material: PLA	Scale: 1:2
	Unit: mm	Sheet No.: 8

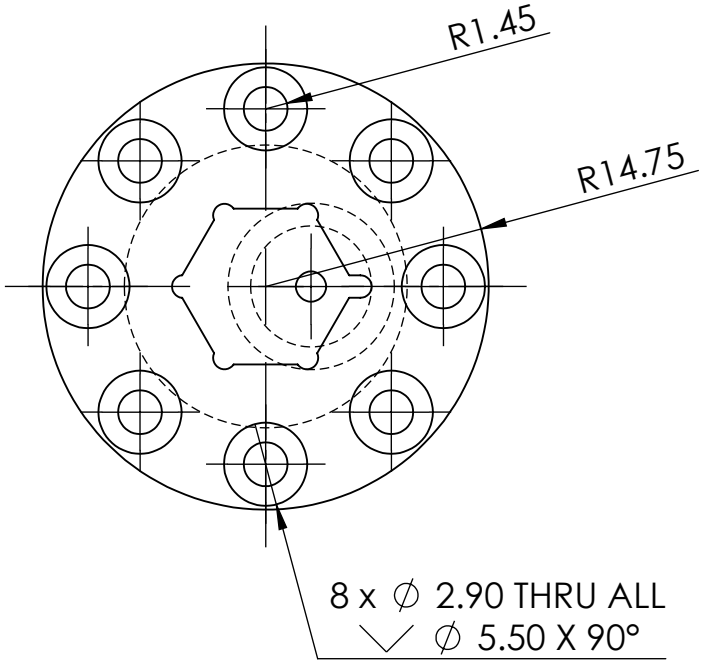

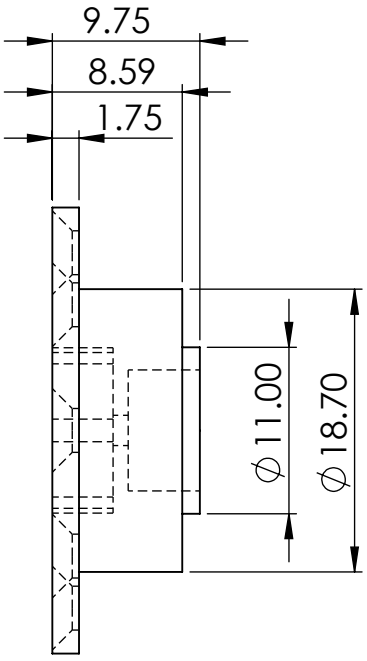

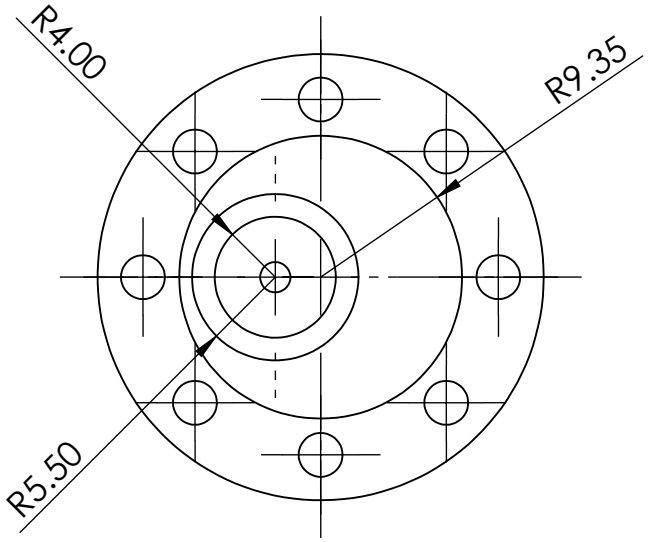

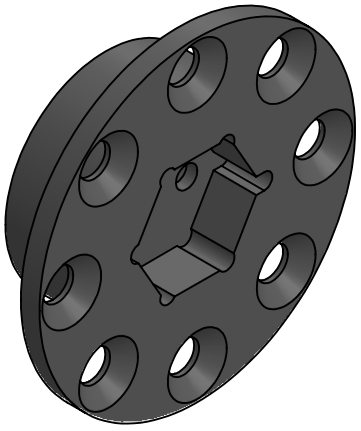

Title: Shaft Cap Eccentric		
	Material: PLA	Scale: 2:1
	Unit: mm	Sheet No.: 9

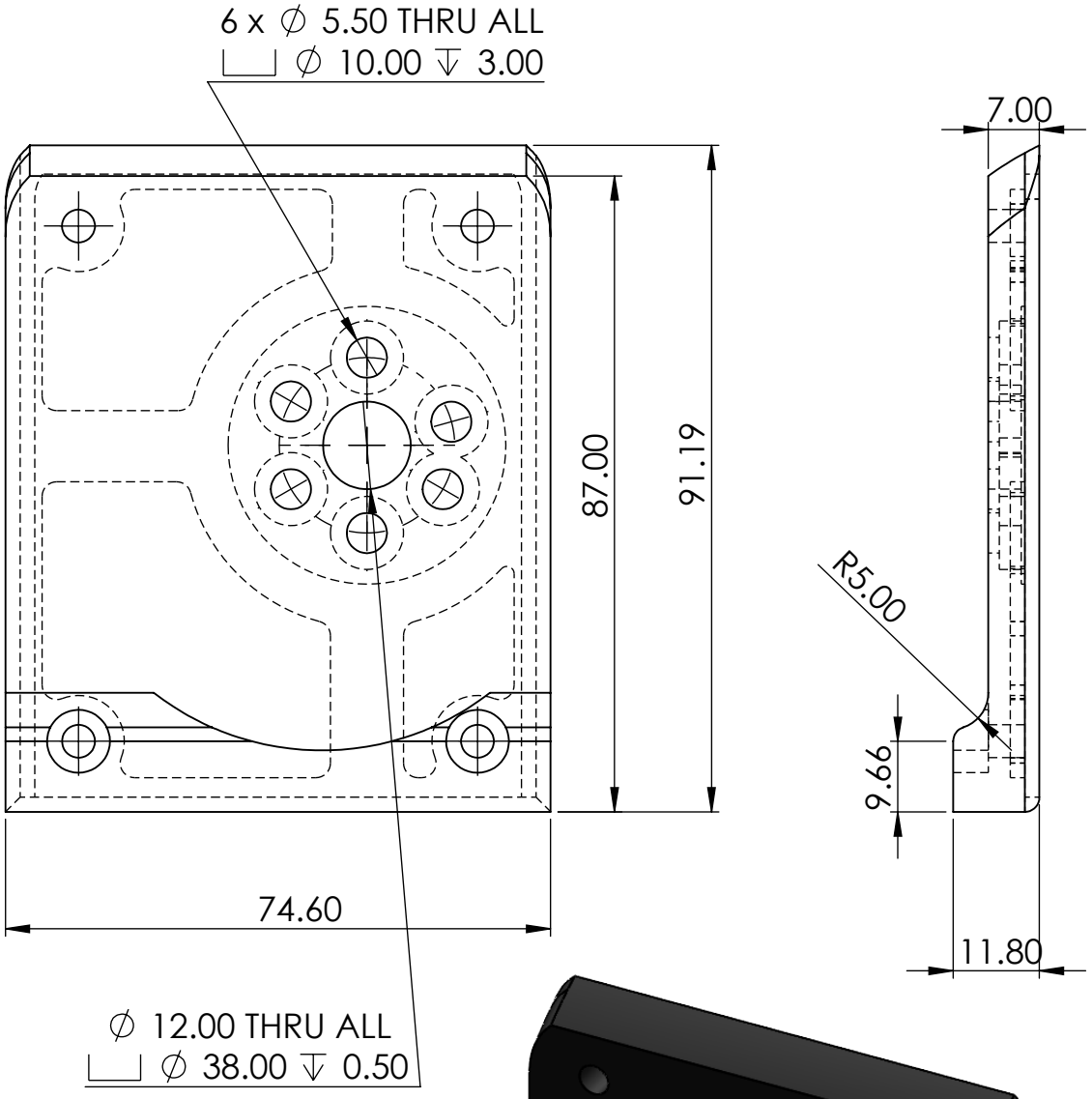

Title: Top Base		
	Material: PLA	Scale: 1:1
	Unit: mm	Sheet No.: 10

APPENDIX B

Table B1: Motor Parameters Corresponding to the Bits

32-19 bit	18 bit	17 bit	16 bit
Reserved value	Motor ID (1 byte)	Motor position (4 byte)	Motor Error Flag (1 byte)
6 bit	5 bit	4 bit	3 bit
Lq current (4 byte)	Id current (4 byte)	Input current (4 byte)	Output current (4 byte)

The motor parameters provided below is used to determine the motor's transfer function:

Table B2: Motor Specifications

Parameter	**Value**
Peak current (AUC)	22.7
K_v (rpm/V)	140
K_t (Nm/A)	0.078
K_e (V/krpm)	7.5
Phase to Phase resistance (mΩ)	202
Phase to Phase inductance (μH)	138
Inertia (gcm^2)	243.5
K_m (Nm/vW)	0.17
Mechanical time constant (ms)	0.81
Electrical time constant (ms)	0.68
Weight (g)	368

The system parameters provided below are used to determine the transfer function of the plant:

Table B3: System Parameter

Parameter	**Value**
Moment of Inertia	0.0039 kgm^2
Mass	1.176(kg)
Distance	150(mm)
Constant	o.5
Gravity	9.8m/s^2

To calculate the stiffness of the spring, we conducted a series of experiments. In the experiment we used mass (m_1) of 680 gram and measured the time take to complete 5 oscillations.

Table B4: Data of Oscillation for Spring Stiffness Calculation for 680 g

SN	**Oscillation**	**Time Period**
1	5	5.75
2	5	6.15
3	5	6.20
4	5	5.65
5	5	5.85

Similarly, an experiment was conducted using a mass (m_2) of 1,080 grams.

Table B5: Data of Oscillation for Spring Stiffness Calculation for 1080 g

SN	**Oscillation**	**Time Period**
1	5	7.61
2	5	7.63
3	5	8
4	5	8.86
5	5	9.68

$$\omega = \sqrt{\frac{k}{m}} \tag{0.89}$$

By performing the calculations above, we calculated the stiffness of the spring to be approximately 250 N/m.

Code: Gain analysis

```
clear();
%%% System Parameters %%%
R = 0.5;
L = 1e-6;
Ts = 0.00010;
wc = pi/5;
%%%
s = tf('s');
z = tf('z', Ts);

% Continuous-time system
sys = 1/(L*s + R);
sys_d = c2d(sys, Ts); % Discretized system

% PI Controller
ki = 1 - exp(-R*Ts/L);
k = R * (wc / (1 - exp(-R*Ts/L)));
controller = k * (1 + ki/(z-1));

% Open-loop system
fp = controller * sys_d; % Use multiplication instead of
   series()
cl = feedback(fp, 1); % Closed-loop system

%%% Bode plots %%%
```

```
figure;
hold on;
bode(controller);
bode(sys_d);
margin(fp);
legend('Controller', 'Plant', 'Return Ratio');
grid on;

%%% Closed-loop step response %%%
figure;
step(cl);
grid on;
```

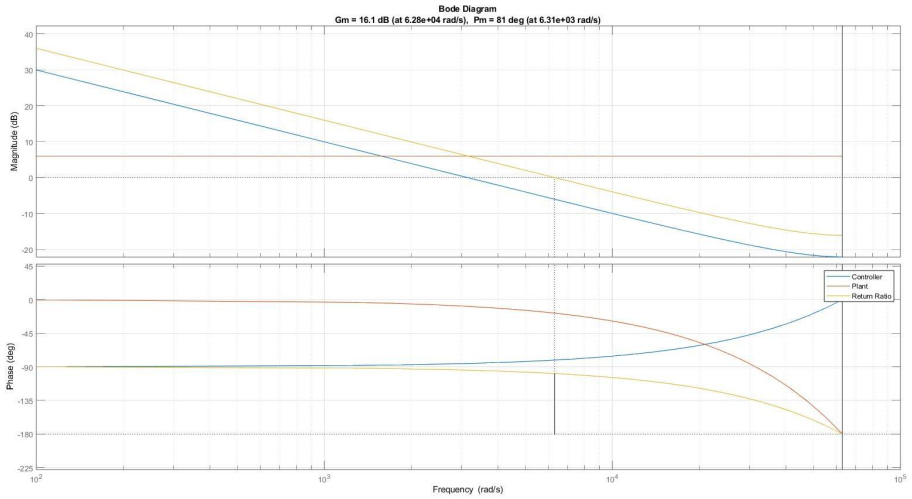

Figure B1: Bode plot

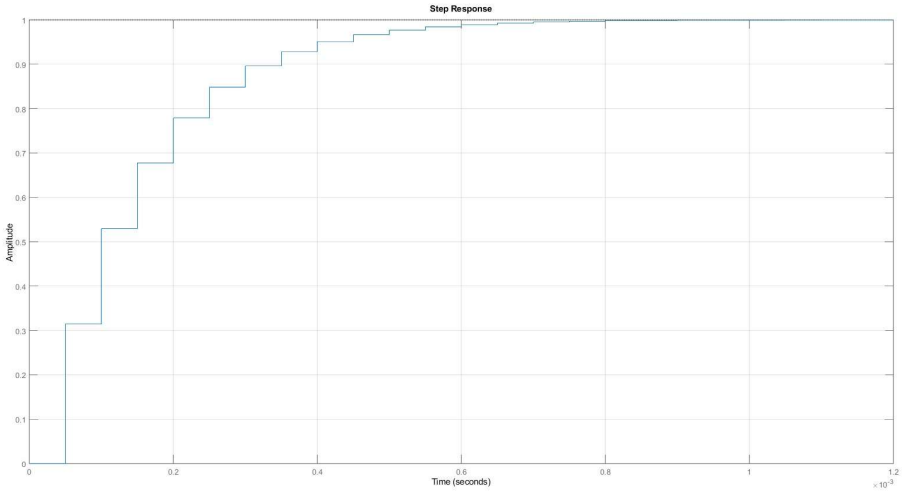

Figure B2: Step response